Environmental Spectroscopy and Biogeochemistry Facility

The Environmental Spectroscopy and Biogeochemistry (ES&B) Facility focuses on environmental molecular science and application of the fundamental concepts of physical chemistry to the study of chemical reactions in heterogeneous natural materials, with an emphasis on soil and subsurface systems. The ES&B Facility staff, along with other Pacific Northwest National Laboratory (PNNL) staff, form a multidisciplinary research team with expertise in chemistry, mineral physics, geochemistry, soil chemistry, microbiology, hydrology, and environmental engineering.

Capabilities

Capabilities are available for materials characterization, aqueous- and solid-phase speciation and reaction/kinetic measurements, analytical environmental chemistry, molecular and thermodynamic geochemical process modeling, and intermediate-scale, reactive-transport studies. Research includes studies on:

- surface chemistry of Fe, Mn, and Al oxides, carbonates, and layer silicates
- redox reactions of organic and metal contaminants with Fe- and Mn-containing mineral solids
- biogeochemistry of Fe(III) and Mn(IV) oxide reduction by bacteria and associated biomineralization processes
- mineral surface structure and dynamics by modeling and microscopy
- sorbate surface structure and dynamics on mineral surfaces by spectroscopy
- reactivity and thermodynamics of contaminants at high ionic strengths
- intermediate scale subsurface flow and transport.

The ES&B Facility consists of seven laboratories that are proximally located to facilitate multi-technique studies. For example, environmental chambers are available with spectroscopic access to allow controlled-atmosphere experiments. These laboratories are located near other instrumentation that is integral to environmental molecular science,

Instrumentation & Capabilities

- Analytical chemistry instrumentation
- Scanning probe microscopy
- Spectrophotometers
- Laser fluorescence microscopy
- Laser spectroscopy and kinetic systems
- Scanning and transmission electronic microscopies
- Laser photoacoustic spectrometer
- Mössbauer spectroscopy
- Electron paramagnetic resonance spectroscopy
- Controlled atmosphere chambers
- Computational geochemical molecular modeling software and hardware
- Hydro- and biogeochemical modeling and software
- Subsurface flow and transport experimental laboratory
- Thermodynamics of aqueous and adsorption reactions

including high-resolution scanning and transmission electron microscopies and a variety of ultra-high vacuum microprobe techniques for surface analyses. The seven ES&B laboratories are describe below.

Optical Spectroscopy Laboratory. Laser-based fluorescence, nonlinear, photoacoustic, and Raman spectroscopies are available to use in investigations of aqueous and interfacial reactions. Kinetic studies ranging from stopped-flow to ultra-fast optical pump-probe methods can be performed. Cryogenic capabilities for enhanced spectroscopic studies of heterogeneous materials are available. Specially designed sample cells allow high-pressure and high-temperature studies, as well as spectroscopic studies of particle suspensions.

Infrared Spectroscopy Laboratory. State-of-science Fourier transform (FT) spectrometers enable the study of various mineral-chemistry topics as well as sorbate binding mechanisms at mineral, biotic, and organic interfaces. The modular design of the spectrometers in this laboratory enables rapid changing of detector and beam-splitter combinations so researchers can readily change from the visible (400 to 700 nm) to the near- (770 nm to 2.5 μm), mid- (2.5 to 25 μm), or far-infrared (25 to 1000 μm) ranges of the light spectrum. A vacuum bench equipped with a helium-cooled bolometer and step-scanning capabilities is optimized for far-infrared measurements down to 10 cm^{-1} as well as time-resolved spectroscopy at 10-ns resolution. A nitrogen-purged system equipped with a microscope and temperature-controlled mapping stage (-200 to 600°C) allows spatially resolved infrared measurements at the 60-μm level. A variety of cells are available for analyzing gas, liquid, solid, and slurry samples using a variety of techniques including attenuated total reflectance, diffuse reflectance (DRIFTS), specular reflectance, gas sampling, liquid transmission, solid transmission, and a photoacoustic cell and detector. Raman vibrational analyses can be obtained using the FT-Raman module and Raman microscope.

Mössbauer and Electron Paramagnetic Resonance (EPR) Spectroscopy Laboratory. Mössbauer spectrometers with cryogenic capabilities allow studies of Fe structure and redox chemistry in oxides, clays, and biogeochemical systems. Software incorporating Voigt-line fitting and quadrupole-splitting distributions enable state-of-science spectral deconvolution and fitting. A continuous-wave, multi-frequency (S, X, and Q bands) EPR spectrometer equipped with helium-cooled cryostats and a stop-flow-freeze quench system allows studies of free-radical reactions and electronic environments of paramagnetic species in solids and suspensions and at surfaces.

Imaging Microscopy Laboratory. Optical and scanning-probe microscopies are available for particle imaging from millimeter to nanometer scales. An inverted optical microscope is available for time-resolved fluorescence imaging in a broad temperature range. Expertise is also available in the characterization of processes of microbial reduction and biogenic mineral formation by high-resolution transmission electron microscopy, involving lattice imaging, selected area diffraction, and energy dispersive spectrometer analysis. A state-of-science scanning-probe microscopy facility has been developed for imaging water-wet samples and microbe-water and mineral-microbe interfaces, and for characterizing a wide variety of environmental materials.

Environmental Analytical Chemistry Laboratory. A wide variety of instrumentation is available for quantification of inorganic and organic contaminants and their reaction, transformation, or degradation products. State-of-science separation instruments, including gas and high-performance liquid chromatographs as well as capillary electrophoretic separators coupled with mass spectrometry, are available to users engaged in diverse research activities. An inductively coupled plasma mass spectrometer with laser ablation for solids analysis and a collision cell for improved detection of oxide-interfering elements (e.g., Fe) is available for broad-spectrum, high-sensitivity inorganic analyses.

Computational Geochemistry. Multiple workstations linked to the computational infrastructure of W.R. Wiley Environmental Melocular Sciences Laboratory (EMSL) are available for graphics, simulations, and modeling to support research in the ES&B Facility. Experts are available to perform molecular dynamics and electronic structure calculations as either a stand-alone activity or in support of experimental or spectroscopic measurements. Thermodynamic and kinetic geochemical codes also are available to users, as are multidimensional geochemical reaction/transport codes for numerical experiments or simulations of the intermediate-scale flow and transport experiments described below.

Subsurface Flow and Transport Experimental Laboratory. This new laboratory (Figure 1) is uniquely equipped for intermediate-scale (i.e., meter-scale) experimentation in single-fluid and multifluid (air-water, air-nonaqueous phase liquid [NAPL]-water, NAPL-water) porous media systems. These distinctive experimental systems allow testing of basic theories of flow and transport; studies of coupled processes involved with microbial, reactive chemical, or colloid transport; and experimental simulation of subsurface remediation scenarios. Close linkages exist between this center and the modeling facility, as pre- and post-experiment modeling are key to experimental design and interpretation.

Figure 1. The Subsurface Flow and Transport Experimental Laboratory enables novel flow and transport studies. Here, scientific consultant Mark Oostrum, PNNL, and user Jacob Dane, Auburn University, Auburn, Alabama, prepare an experiment to investigate a complex dense nonaqeous phase liquid (DNAPL) – a composition similar to the mixture disposed of at the Hanford site in the 1950s and 1960s and now present in Hanford subsurface heterogeneous materials.

Upgrades

Mössbauer Laboratory. The Mössbauer Laboratory was rearranged to avoid the possibility of creating magnetic field effects when the future applied-field Mössbauer spectrometer is installed in the proximity of existing spectrometers. Two cryostats, electronics, sources, computers, and data acquisition systems were ordered and installed; framing systems for all the three Mössbauer setups were designed and installed; and framing/shielding was optimized to allow installation of permanent radiation shielding. These upgrades bring the total number of Mössbauer spectrometers to four: one room temperature instrument, two 4.2-K instruments, and one 10-K instrument. The cryostats allow variable temperature studies as low as 4.2 K, which is a critical capability in characterizing speciation, mineralogy, and magnetic properties of Fe-containing nanoparticles.

Pressure-Monitoring Flow Cell. A pressure-monitoring flow cell (Figure 2) was designed and built for the Subsurface Flow and Transport Experimental Laboratory. The cell has several monometer ports to measure the build-up of gas pressures. Initial experiments will examine the fate and transport of nitrogen gas produced *in situ* by indigenous nitrate-reducing organisms.

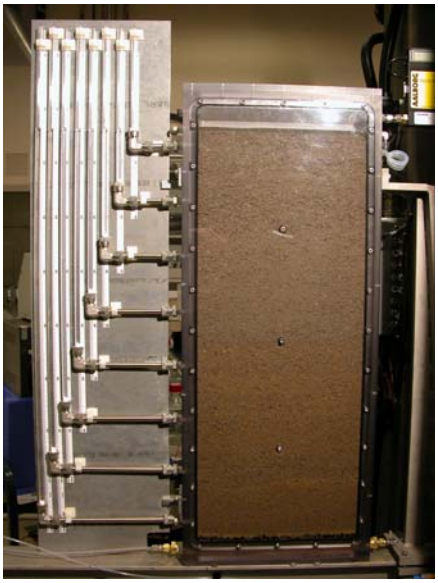

Figure 2. The pressure monitoring flow cell has several monometer ports to measure the build-up of gas pressures.

Optical Microscope. A Nikon TE-2000U inverted optical microscope has been integrated with the SpectraPhysics MOPO-730 nanosecond laser system and an Acton-Research MicroSpec 2156i spectrograph fitted with a Roper Scientific Research intensified charge coupled device detector. Currently, the system is being tested for cryogenic fluorescence studies of heavy metal radionuclides such as U, Eu, and Cm that are present in contaminated Hanford sediments. This system can potentially be used to perform time-resolved fluorescence imaging and to subsequently acquire time-resolved fluorescence spectra of specific areas of interest on the fluorescence image.

Laser Installation. A picosecond diode-pumped Nd:YAG laser was installed. The output of the laser is 2 Watts of 532 nm pulses at a repetition rate of 76 MHz and a pulse width of 12 psec. The output of this laser can be used to synchronously pump a cavity-dumped dye-laser, providing tunable picosecond pulses in the visible (560 to 760 nm) and near-ultraviolet (280 to 380 nm) regions through second harmonic generation. This laser combination can be used to measure luminescence lifetimes by coupling with either the Hamamatsu streak camera (time resolution of approximately 10 psec) or the time-correlated single photon counting system (time resolution of approximately 50 psec). Present experiments involve measuring the fluorescence lifetimes of doped, inorganic nanoparticles.

Future Directions

In 2005, the ES&B Facility will be involved in the EMSL Biogeochemistry Grand Challenge. Consulting scientists in the areas of fluorescence spectroscopy, imaging microscopy (atomic force/scanning electron/transmission electron microscopy [AFM/SEM/TEM]), spectroscopy, and molecular modeling will be involved. Research will also continue in the subsurface flow and transport, actinide geochemistry, and computational geochemistry.

Additionally, the facility has several capability developments planned for the coming year.

- Laser-Induced Breakdown Spectroscopy/Detection (LIBS/LIBD) will be developed for *in situ* investigation of nanoparticulates such as aerosols and nanocolloids and for possible remote chemical analysis of contaminants in hostile environments.
- Applied-field (magnetic) Mössbauer spectroscopy in conjunction with low temperatures will be used to understand (bio)-transformation of Fe(III)-phases in sediments (e.g., Ringold sediment of the Hanford site).
- A small (50-cm) chlorinated solvent resistant flow cell will be designed and built for use in the Subsurface Flow and Transport Experimental Laboratory.

LIBS/LIBD is an emerging analytical capability that offers the prospect of *in situ*, rapid, highly sensitive, and selective detection and analysis of both natural and man-made materials. Recently, there has been a surge in the development of LIBS/LIBD-based techniques, partly because of the availability of more compact and reliable solid-state lasers, broadband high-resolution spectrometers, and sensitive detectors. The intrinsic similarities between LIBS/LIBD techniques and our current laser-induced fluorescence techniques along with the laser systems and detection systems we currently have in the Environmental Spectroscopy Laboratory offer an ideal starting point to develop the LIBS/LIBD capabilities at EMSL and PNNL. The capability may be used by the Catalysis Collaborative Access Team and the Atmospheric Collaborative Access Team.

Low Temperature Applied-Field Mössbauer Spectrometry. EMSL Mössbauer spectrometers are primarily used to identify, characterize, and quantify Fe(III)-oxides and Fe-containing clays in pristine and contaminated soils and sediments. The spectrometers are also used to study mineralization associated with dissimilatory bacterial reduction of these Fe(III) oxides and Fe-containing clays. This capability, however, is not adequate to fully characterize Fe in other systems of interest, for example biotransformed Fe(II) in reduced sediments, such as Hanford and Oak Ridge sediments. An applied-field (magnetic) Mössbauer spectrometer in conjunction with low temperature will enable understanding (bio)-transformation of Fe(III)-phases in sediments (e.g., Ringold sediment of Hanford Site). The capability is also valuable to current and future EMSL users who need to characterize Fe for applications in other areas, such as catalysts, magnetic materials, and nanoparticles. The Mössbauer Laboratory will help enable the EMSL Biogeochemistry Grand Challenge and the Catalyst Collaborative Access Team.

Small-Scale Flow Cell. Many experiments do not require the use of larger intermediate-scale flow cells. This smaller cell will allow multiple experiments to be conducted in the time it would take to pack a single larger flow cell. This smaller flow cell would also offer increased flexibility to run intermediate-scale experiment under multiple conditions more efficiently and would also allow the testing of ideas and the determination of experimental parameters prior to scaling up to larger flow cells.

Removal of a Dense Nonaqueous Phase Liquid from a Layered Porous Medium by Means of Vapor Extraction Enhanced by Desiccation and Water Table Reduction

JH Dane,[(a)] M Oostrom,[(b)] and TW Wietsma[(c)]

(a) Auburn University, Auburn, Alabama
(b) Pacific Northwest National Laboratory, Richland, Washington
(c) W.R. Wiley Environmental Molecular Sciences Laboratory, Richland, Washington

Flow cell experiments are used to investigate the flow and transport behavior of liquids containing organic chemical contaminants, such as carbon tetrachloride, that were disposed of at the Hanford Site in the 1950s and 1960s. This work will advance our understanding of soil-vapor extraction techniques that could be used to clean up contaminated sites.

Vapor extraction is an *in situ* soil-cleaning process designed to remove volatile organic compounds (VOCs) from the unsaturated zone of soil (i.e., the vadose zone). Some of the more commonly occurring VOCs that have contaminated soil and groundwater are the dense nonaqueous phase liquids (DNAPLs) trichloroethylene, perchloroethylene, and carbon tetrachloride. These contaminants can occur in free, residual, and/or trapped states in the liquid phase; in the solid phase by means of adsorption, especially to organic matter; in the aqueous phase when dissolved; and/or in the gas phase.

Any remediation treatment will benefit from a proper analysis of the liquid and gaseous flow regimes and the fate of contaminants in the subsurface environment. The model must, however, give a true description of all physical, chemical, and biological phenomena. Therefore, models must be continuously tested by comparing their results with quantitative data obtained during controlled experiments that mimic real situations. Based on known knowledge gaps and a desire to enhance our understanding of DNAPL fate in the environment and subsequent cleanup activities, we formulated the following objectives for this project:

- Investigate the infiltration and redistribution of a DNAPL in a variably saturated, layered porous medium in an intermediate-scale experiment.
- Remove non-trapped DNAPL present in the vadose zone using wet vapor extraction.
- Remove DNAPL trapped in both the vadose and saturated zones by reducing the water-table level and employing dry vapor extraction.
- Model the processes of the first three objectives using the Subsurface Transport Over Multiple Phases (STOMP) computer model and compare the numerical and experimental results.

To perform the experimental part of the study, four sloped layers were embedded in an otherwise mostly homogeneous porous medium. As shown from top to bottom in Figure 1, the layers consisted of fine, coarse, fine, and coarse material. The purpose of this layering was to obtain a clear picture of DNAPL behavior at sloped interfaces of materials with different pore sizes and, consequently, with different hydraulic properties such as permeability and displacement pressures. The layers were also thought to affect any remediation efforts. To mimic a real situation, the materials for the layers were obtained from the U.S. Department of Energy's Hanford Site in southeastern Washington.

Figures 1 through 4 show a series of four time-lapse photographs taken as the experiment proceeded. Initially (Figure 1), the DNAPL infiltrated very much as a sphere, similar to the infiltration of water from a point source into dry soil. When the DNAPL reached the first fine layer, it began to spread to the left and right and edged over both ends of the layer (Figure 2). During the subsequent redistribution, the DNAPL continued to move straight down on the left side of the layers (i.e., the higher ends of the layers) but followed a more intriguing path at the lower ends. The first coarse layer, which was unsaturated, accepted the DNAPL after some spreading occurred at the boundary, again indicating the DNAPL moved as a wetting fluid in the unsaturated zone. When it reached the first coarse layer, the DNAPL moved straight down (Figure 2) because of the diminished capillary action of the larger pores. As time passed, the DNAPL on the left side reached the capillary fringe (i.e., the saturated zone) and apparently was under enough pressure to displace the water (Figure 3). Meanwhile, on the right side of the layers, free DNAPL moved through the coarse layer, accumulated on top of the second fine layer, and began to flow down the boundary until it spilled over the edge (Figure 3). It then spread somewhat on top of and moved into the second coarse, unsaturated layer. As with the first coarse layer, the DNAPL subsequently moved straight through and entered the underlying finer material without much delay. The DNAPL again affected the surface tension of water, because the capillary fringe on the right side also had begun to collapse (Figure 3). The final DNAPL

Figure 1. The four sloping layers, from top to bottom, consisted of fine, coarse, fine, and coarse material. The red sphere is the initial simulated DNAPL spill.

Figure 2. When the DNAPL reached the first layer (fine material), it spread to the left and right and then edged over both ends. When it reached the second layer (course material) on the right, the DNAPL moved through the layer.

distribution, for which we assumed static equilibrium, is shown in Figure 4. It clearly shows the collapse of the capillary fringe, which was attributed to a reduction of the surface tension of water caused by DNAPL diffusion in the liquid phase.

During the infiltration and initial redistribution of a DNAPL in an unsaturated porous medium, its flow is so rapid that the best way of documenting its behavior is by obtaining photographs (Figures 1 through 4). However, when static equilibrium of both water and DNAPL was obtained, gamma-radiation attenuation was used to determine liquid saturations at 1150 more or less evenly distributed locations. Additional gamma-radiation scans were obtained to quantify the removal of carbon tetrachloride during the vapor extraction procedures. The gamma data and analysis of the extracted vapor samples will be modeled using STOMP to compare numerical and experimental results.

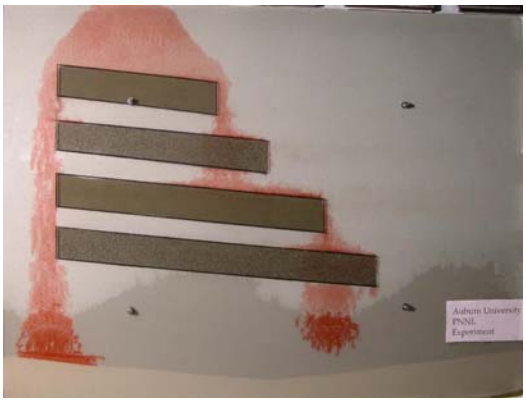

Figure 3. On the right side (the lowest sides of the layers), the DNAPL flowed down in a stair-step pattern. First, it spread across the top and down the right side of the first layer (fine material); then it flowed through the second layer (course material). When the DNAPL encountered the third layer (fine material), it again flowed across the top and down the right side. Finally, when it reached the last layer (coarse material), the DNAPL flowed through the layer.

Figure 4. Near the final DNAPL distribution, full collapse of the capillary fringe was observed. This collapse was attributed to a reduction of the surface tension of water caused by DNAPL diffusion in the liquid phase.

Uranium Immobilization by Sulfate-Reducing Biofilms

H Beyenal,[(a)] RK Sani,[(b)] BM Peyton,[(b)] AC Dohnalkova,[(c)] JE Amonette,[(c)] and Z Lewandowski[(a)]

(a) Montana State University, Bozeman, Montana
(b) Washington State University, Pullman, Washington
(c) Pacific Northwest National Laboratory, Richland, Washington

Uranium mining and processing for use in nuclear weapons and power plant fuel have left thousands of sites with toxic levels of this actinide in soil and groundwater. Understanding uranium precipitation by metal-reducing bacteria may lead to improvements in bioremediation processes.

In this research, hexavalent uranium [uranium (VI)] was immobilized using biofilms of the sulfate-reducing bacterium (SRB) *Desulfovibrio desulfuricans* G20. The dynamics of uranium immobilization in the SRB biofilms were quantified by estimating:

- microbial activity in the SRB biofilm, defined as the hydrogen sulfide production rate and estimated from the hydrogen sulfide concentration profiles measured using microelectrodes across the biofilms
- the concentration of dissolved uranium in the solution
- the mass of uranium precipitated in the biofilm.

Results of this research suggest that uranium was immobilized in the biofilms enzymatically and chemically, the latter by reacting with microbially generated hydrogen sulfide. Selected-area electron diffraction pattern and crystallographic analysis of transmission electron microscope lattice-fringe images confirmed the structure of precipitated uranium as being uraninite.

Transmission electron microscope imaging and analysis (Figures 1 and 2, respectively) were used to investigate the reduced uranium (IV)-containing minerals associated with the bacterial cells. Cross-sectional transmission electron microscopy is the only method that provides a view of the inside of a bacterial cell and allows researchers to study the exact location of the newly formed biominerals. To assist with this research, the W.R. Wiley Environmental Molecular Sciences Laboratory (EMSL) at Pacific Northwest National Laboratory provided a unique capability for examining these redox-sensitive systems following a protocol for anaerobic sample processing developed by EMSL researchers. In addition, a state-of-the-art, high-resolution transmission electron microscope located in EMSL coupled with an energy-dispersive spectroscopy system provided atomic resolution imaging and elemental analysis of structures on the nanolevel, which was critical for their identification.

This research allowed scientists from the Multiphase Environmental Research group at Washington State University in Pullman, Washington, to understand uranium precipitation and cycling by dissimilatory metal-reducing bacteria in their experimental setup.

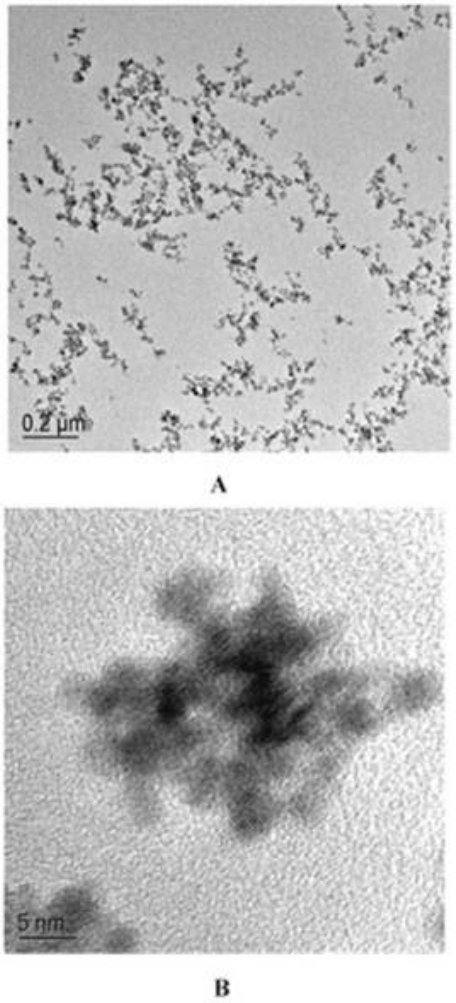

Figure 1. A) Transmission electron microscope images of unstained thin sections from uranium (VI) incubated with sodium sulfide, illustrating the production of reduced uranium. B) High-resolution transmission electron microscope image of uranium precipitates. The average particle size of the newly formed biogenic uraninite was 4 nm.

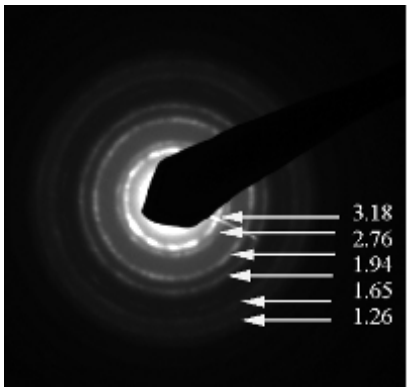

Figure 2. Electron diffraction pattern of the uranium particles precipitated by sodium sulfide showing rings characteristic for nanocrystalline material and with d-spacing values that are in good agreement with the listed nonbiogenic uraninite diffraction data.

A Theoretical and Experimental Investigation of X-Ray Photoelectron Spectra for Chromium and Uranium

ES Ilton[(a)] and PS Bagus[(b)]

(a) Pacific Northwest National Laboratory, Richland, Washington

(b) University of North Texas, Denton, Texas

This study will help us understand how transition metals and actinides sorb to minerals found in the environment. The chemical state of the absorbed species will determine their toxicity and mobility in the soil.

We have developed relativistic *ab initio* models for the 2p and 3p spectra of chromium ions in embedded CrO_6 clusters of varying symmetry (Bagus et al. 2004a). The models for chromium 2p predict the relative energies of the multiplets, but more work is required before relative intensities can be calculated. In related work, we discovered a new atomic, many-body effect that significantly improves comparison of theory for manganese 3s with experiments (Bagus et al. 2004b). We coined the term 'frustrated auger configuration,' or FAC, to provide an abbreviated description of the effect. We also have begun to investigate the influence of bonding environment on the 4f spectra of uranium ions. Theoretical models will help to determine the uniqueness of spectral features for uranium (IV), uranium (V), and uranium (VI) that help identify uranium oxidation states. For example, theoretical multiplet and satellite intensities and energies for the uranium 4f lines of the free U^4 and U^{5+} ions have been calculated (Figure 1). Comparison of the calculated spectrum for U^{4+} with a spectrum for UO_2 indicates that intra-atomic effects are first order. However, inter-atomic effects appreciably decrease the multiplet splitting. Further, theory does not predict the 7-eV satellite that is diagnostic of U^{4+} in UO_2. This finding is consistent with experimental evidence for an inter-atomic origin of this satellite.

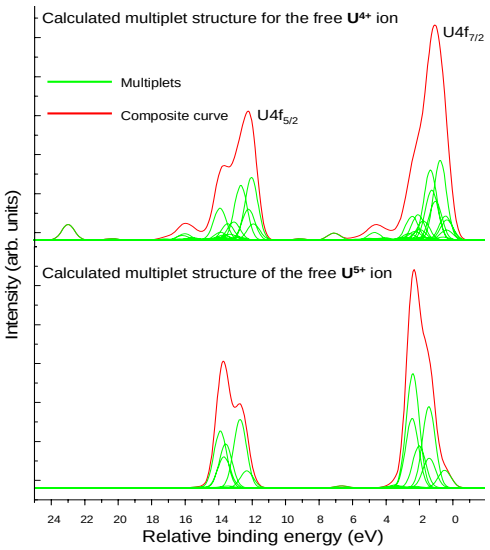

Figure 1. Theoretical uranium 4f x-ray photoelectron spectroscopy for the free U^{4+} ion (upper graph), and for the free U^{5+} ion (lower graph).

References

Bagus PS, ES Ilton, and JR Rustad. 2004a. "Ligand Field Effects for the 3p Photoelectron Spectra of Cr_2O_3." *Physical Review B, Condensed Matter and Materials Physics* 69:205112.

Bagus PS, R Broer, and ES Ilton. 2004b. "A New Near Degeneracy Effect for Photoemission in Transition Metals." *Chemical Physics Letter*s 394(1-3):150-154.

High-Pressure Fluorescence and Optical Imaging of Anthracene Single Crystals: Effect of Nonhydrostaticity

ZA Dreger,[(a)] E Balasubramaniam,[(a)] YM Gupta,[(a)] and AG Joly[(b)]
(a) Washington State University, Pullman, Washington
(b) Pacific Northwest National Laboratory, Richland, Washington

The application of high pressure to a molecular solid is a powerful method for changing the physical and chemical properties of the material. These effects include changes in the vibrational and electronic structure as well as changes in crystal phase or defect formation. Perhaps unexpectedly, these changes depend not only on the crystal structure of the solid but also on the quality of the crystal.

The broad objective of this research is to examine the origin and nature of electronically accessible structural defects in compressed anthracene single crystals. Specifically, we want to understand the role of nonhydrostatic stresses in formation and modification of structural defects. To pursue this objective, we complemented our previous studies with measurements of fluorescence decay using research resources available in the W.R. Wiley Environmental Molecular Sciences Laboratory.

We performed four sets of fluorescence decay measurements of anthracene single crystals under high pressures in a diamond anvil cell, employing either 360-nm or 532-nm excitation lines from a mode-locked Nd:YAG laser. A time-correlated, single-photon counting system with a multichannel-plate photomultiplier tube was used to detect the fluorescence decays. We obtained pressure dependence of fluorescence decays under hydrostatic and nonhydrostatic conditions using excitation within the singlet (360-nm) and triplet (532-nm) states absorption. In hydrostatic conditions, a gradual increase of nonradiative rates with increasing pressure was observed. However, under nonhydrostatic conditions, the fluorescence decays changed their character, exhibiting an apparent build-up component (Figure 1). The occurrence of the build-up component in the fluorescence decays was correlated with other changes detected in fluorescence spectra and optical images. We propose that the non-hydrostatic stresses generated a range of structural defects in the compressed crystal, with the fluorescence decay measurements helping to determine the nature of the defects.

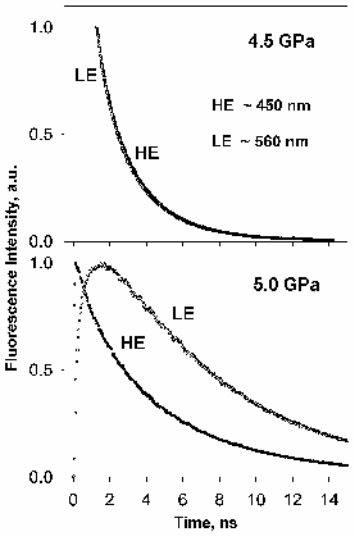

Figure 1. Fluorescence decay curves for the low-energy (LE) and high-energy (HE) parts of the fluorescence spectra at hydrostatic and nonhydrostatic pressures (4.5 GPa and 5.0 GPa, respectively).

Addressing Complexity at Rough Mineral Surfaces: Basic Dissolution of Quartz

SV Yanina,[(a)] KM Rosso,[(a)] P Meakin,[(b)] and JR Rustad[(c)]
(a) Pacific Northwest National Laboratory, Richland, Washington
(b) Idaho National Laboratory, Idaho Falls, Idaho
(c) University of California at Davis, Davis, California

Surface roughness is an important factor in growth, dissolution, and adsorption experiments, but the relationships between these processes and roughness are complex. This research focuses on developing a new strategy for understanding the properties of complex surface topologies and on providing mechanistic insights into the dissolution of complex surfaces of common sedimentary materials.

The surfaces of minerals in natural settings exhibit significant degrees of morphological heterogeneity on scales from 1 to 1000 nm. Surface roughness and its time-dependent evolution are important factors in growth, dissolution, and adsorption experiments, but because of their inherent complexity, the relationships between these processes and roughness have been difficult to quantify. Furthermore, roughness can influence surface reactivity in a manner that is distinctly different from simple surface area arguments because it has a length-scale dependence ranging from the microscopic scale to the mesoscopic scale. We have begun to compile certain long-standing tools to develop a new strategy to quantitatively treat the evolution of rough surfaces. In this report, we discuss our initial application of this strategy to the dissolution of quartz surfaces.

Atomic force microscopy was used to document the development of dissolution features on flat quartz (100) and (101) surfaces from exposure to aqueous potasium hydroxide solutions (pH ~12) under hydrothermal conditions (127°C). Not surprisingly, dissolution initially proceeds by the nucleation and growth of faceted etch pits. At finer-length scales of observation, such as 1 micron, the surface topography is initially dominated by step-and-ledge features and randomly arranged small etch pits (Figure 1). At larger observation scales, the surface topography is initially dominated by the emergence of large etch pits on what appears to be a flat surface; step-and-ledge features are effectively beyond the lateral image resolution at 50-micron image sizes.

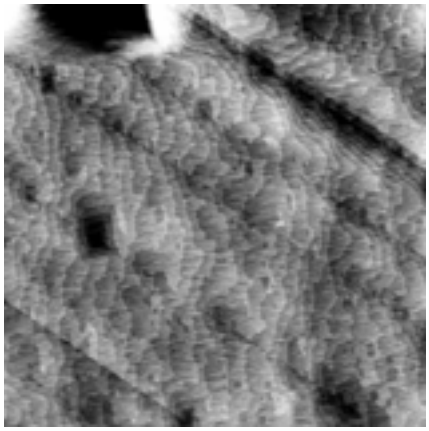

Figure 1. Atomic force microscope image of the development of fine-scale etch features on quartz (100). The image size is 1 × 1 micron. At this observation scale, dissolution is observed to proceed by etch pit growth and step retreat. Measurements were made at pH 7 in a PIPES-buffered basal medium.

As dissolution progresses on the (100) surface, two kinds of features evolve from the coalescence of etch pits. Smaller etch pits with loci that appear to be aligned on shallow structural defects arranged in

a linear fashion coalesce to form linear tracks across the surface (Figure 2). Larger etch pits can coalesce with each other or intersect and eradicate linear tracks. The larger etch pits are associated with dislocations that run deep into the subsurface. Hence, all major dissolution features originate at extended structural defects where they intersect the surface plane. These dissolution features are likely to be dislocations but could also include planar defects and/or twin boundaries. After approximately 200 hours of dissolution, the progressive growth of all etch features in parallel imparts a 'refaceting' of the surface, yielding a complex surface topography that is vertically rough on scales of hundreds of nanometers.

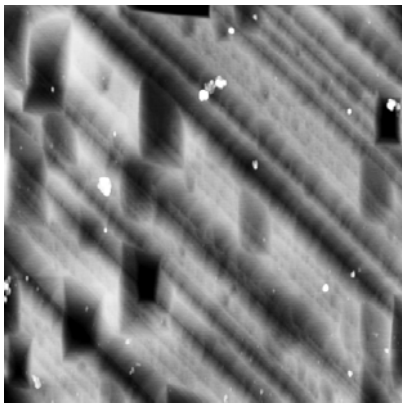

Figure 2. Atomic force microscope image of the development of large-scale etch features on quartz (100) after 60 hours exposure to potassium hydroxide solution under hydro-thermal conditions. The image size is 10 x 10 microns. At this observation scale, dissolution is observed to proceed by growth and coalescence of large etch pits and linear etch 'tracks.'

Clearly the largest control on the manner in which the surface topography evolves is the nature and arrange-ment of defects in the structure. Presumably, the final surface topography and roughness would be difficult to predict without prior knowledge of the structural details pertaining to all defects present. However, it is possible that not all details would have to be known to be able to describe how the essential characteristics of the surface can be obtained. We are testing this idea by computer simulation. Using kinetic Monte Carlo methods, we are generating simulated etched-surface topographies for the case of the presence of multiple linear defects. The defects are defined with a particular strain/stress field to be consistent with either screw or edge dislocations using the theory of linear elasticity. The defects are ran-domly arranged in a 4096 × 4096 field of fundamental mineral 'building block' units (Figure 3). To date, the simulations have demonstrated that there is an energetic 'window' in terms of bond-breaking activation energies in which the surface will coarsen, and the coarsening will depend less on defect arrange-ment and more on density. This finding suggests that the evolution of surface roughness can be described without detailed knowledge of the arrangement of defects. Hence, our current effort is focused on integrating experimental and theorical approaches as the ultimate strategy for understanding surface complexity.

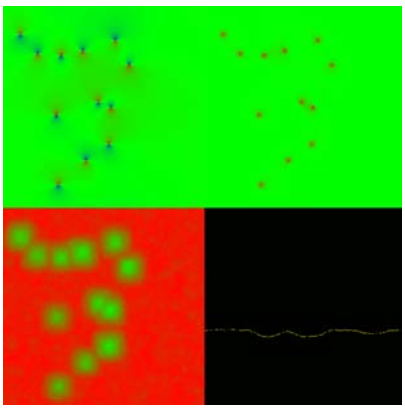

Figure 3. Stress/strain fields (upper left), energy density (upper right), height field (lower left), and height profile (lower right) in one Monte Carlo simulation of dissolution incorporating multiple interacting dislocations.

Copper Sorption Mechanisms on Smectites

DG Strawn,[(a)] NE Palmer,[(a)] LJ Furnare,[(a)] C Goodell,[(a)] JE Amonette,[(b)] and RK Kukkadapu[(c)]

(a) University of Idaho, Moscow, Idaho
(b) Pacific Northwest National Laboratory, Richland, Washington
(c) W.R. Wiley Environmental Molecular Sciences Laboratory, Richland, Washington

Spectroscopic tools can be used to determine the mechanisms by which metals sorb to minerals in soils and sediments. This work used two complementary spectroscopic techniques to explore how copper sorbs to smectite, a common clay-size mineral. The information gained from this study will help researchers improve their models of the fate and transport of copper in soils.

Because of the importance of clay minerals in metal sorption, many studies have attempted to derive mechanistic models that describe adsorption processes. These models often include several different types of adsorption sites, including permanent charge sites and silanol and aluminol functional groups on the edges of clay minerals. To provide a basis for development of adsorption models, it is critical that molecular-level studies be done to characterize sorption processes. In this study, x-ray absorption fine structure (XAFS) spectroscopy at the Stanford Synchrotron Radiation Laboratory and electron para-magnetic resonance (EPR) spectroscopy at the W.R. Environmental Molecular Sciences Laboratory were used to study copper (II) sorption on smectite clays using suspension pH and ionic strength as variables.

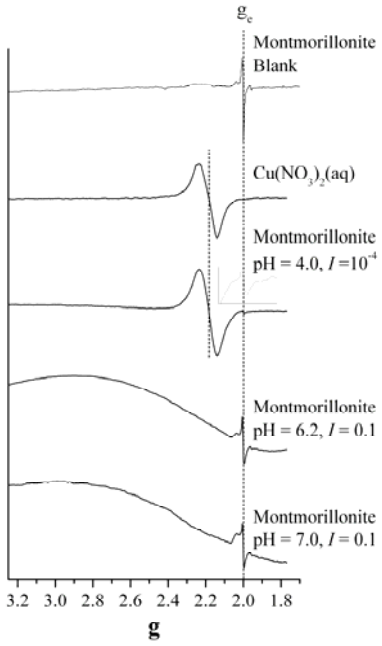

Figure 1. EPR spectra of copper sorbed on montmorillonite as a function of pH and ionic strength. g_e is the free electron resonance at 2.003. A montmorillonite blank sample (no copper) and aqueous copper (II) EPR spectra are shown for reference. The inset on montmorillonite is zoomed in to show features because ordinate scales are different for each spectra. The spectra for high (I=0.1) samples suggest that copper is not sorbed by inner sphere complexation, but instead exists as multinuclear complexes.

At low ionic strength, results suggest that copper sorbs in the interlayers and maintains its hydration sphere. At high ionic strength, copper atoms are excluded from the interlayer and sorb primarily on the silanol and aluminol functional groups of the montmorillonite or beidellite structures. Interpretation of the results from EPR spectroscopy (Figure 1) and XAFS spectroscopy provides evidence that multinuclear complexes are forming.

An example of the copper complexation mechanism on smectite minerals is illustrated in Figure 2. These complexes are consistent with observed sorption on mica and amorphous silicon dioxide, yet are inconsistent with previous spectroscopic results for copper sorption on montmorillonite. The results reported in our paper (Strawn et al. 2004) provide mechanistic data that will be valuable for modeling surface interactions of copper with clay minerals and predicting the geochemical cycling of copper in the environment.

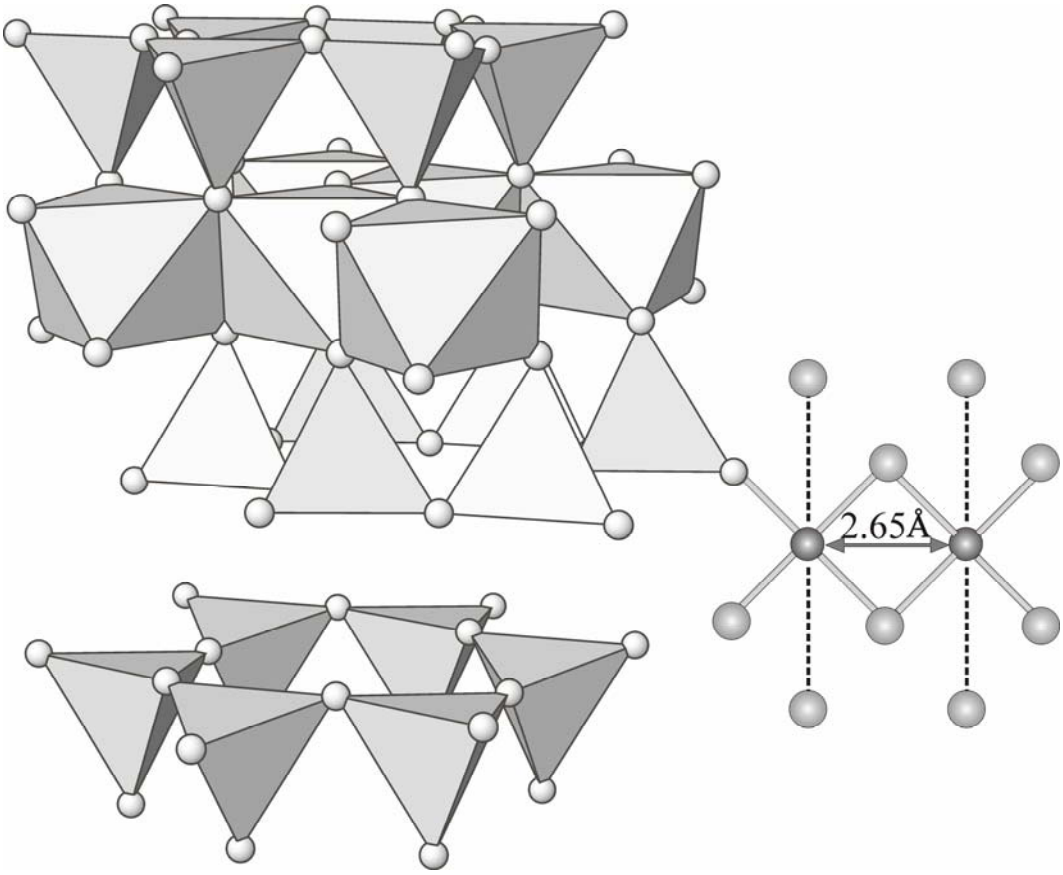

Figure 2. Illustration depicting possible copper complexation mechanisms on smectite clays based on results from this study.

Reference

Strawn DG, NE Palmer, LJ Furnare, C Goodell, JE Amonette, and RK Kukkadapu. 2004. "Mechanisms of Copper Sorption on Smectites." *Clays and Clay Minerals* 52(3):321-333.

Self-Consistent Self-Interaction Corrected Density Functional Theory Studies of Hematite

K Tsemekman,[(a)] H Jonsson,[(a)] and EJ Bylaska[(b)]
(a) University of Washington, Seattle, Washington
(b) Pacific Northwest National Laboratory, Richland, Washington

New theories are being developed to study defect sites in oxides, which can negatively affect the properties of ceramics and semiconductors as well as remediation processes at mineral surfaces.

The structure and mobility of the polaronic state in hematite, which is formed by supplying the system with an additional electron, is relevant to both catalysis and environmental chemistry. It is believed that the electron interacts with the lattice vibrations, polarizes the ions, and may get trapped in local lattice distortions. Such a trapped electron forms a polaron. If the charge is strongly localized, the structure is called a 'small polaron.' It is well known that this type of defect in oxides (i.e., polarons) contains strong electron correlations not described by standard density functional theory (DFT) approaches. The solutions of these defects are inherently delocalized and are not localized via a Wannier transformation. Several methods to improve various failures of DFT proposed in the literature, such as local density approximation plus a Hubbard U term (LDA+U) or self-interaction corrections (SICs), show great promise in describing defects with strong electron correlations.

We have recently developed a framework for the self-consistent calculation of SIC to pseudopotential plane-wave DFT (PSPW). The technique implements the original method of Perdew and Zunger and combines two procedures: 1) construction of maximally localized Wannier functions (MLWFs), a procedure by Marzari and Vanderbilt and to Silvestrelli, and 2) direct minimization of the DFT+SIC total energy functional. The technique developed can be employed in PSPW-DFT methods without adding significant expense. Furthermore, atomic forces and stresses are straightforward to implement, making the approach applicable to both confined and extended systems as well as to *ab initio* Car-Parrinello molecular dynamic (CPMD) simulations. This method has been applied to several systems for which standard DFT methods do not work well.

Very few studies have been performed to date on polarons in hematite. Previous DFT calculations predicted a delocalized polaron; however, cluster simulations within the Hartree-Fock approximation showed a high degree of localization. In our calculations, we saw the full complexity of this problem. Standard DFT calculations indeed predict a delocalized

polaron (Figure 1a): the electronic state of an additional electron lies at the bottom of the conduction band. DFT-SIC calculations in the perfect crystal structure also show a significant degree of delocalization, although the polaron from the DFT-SIC calculation is much more localized than that from the DFT calculation (Figure 1b). To consistently describe the polaron, lattice distortions must be considered. Direct relaxation of the combined electronic and ionic system does not result in stronger charge localization. We explain this effect by the presence of several local minima on the energy landscape typical of complex spin systems. To explore this energy landscape, we implemented DFT-SIC *ab initio* CPMD in the NWChem package. The final state obtained in such CPMD simulation has a perfectly localized polaron (Figure 1c). It is clear that the origin of this state is a d-orbital on one of the iron atoms. As such, the polaron transforms Fe^{3+} into a Fe^{2+} ion.

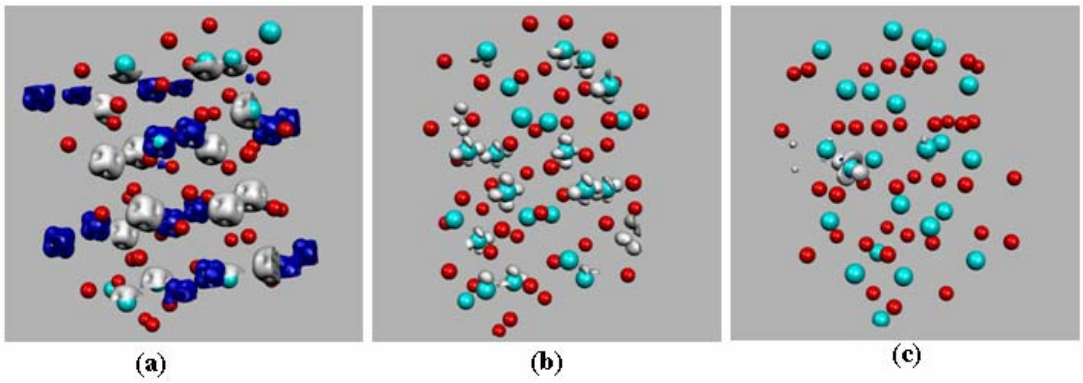

Figure 1. Hematite polaron calculations. Change in spin density induced by the extra electron for (a) delocalized polaron predicted by DFT, (b) delocalized polaron predicted by DFT-SIC without structural relaxation, and (c) localized polaron predicted by DFT-SIC after CPMD (white is spin up, blue is spin down, red atoms are oxygen, and blue atoms are iron).

Influence of Calcite on Uranium (VI) Adsorption to a Subsurface Sediment from the Hanford Site

W Dong,[(a)] WP Ball,[(a)] C Liu,[(b)] Z Wang,[(b)] AT Stone,[(a)] and JM Zachara[(b)]
(a) Johns Hopkins University, Baltimore, Maryland
(b) Pacific Northwest National Laboratory, Richland, Washington

Thousands of sites across the United States contain high levels of uranium contaminants from mining and processing activities. The presence of calcite or other salts, as well as the pH level, can significantly affect the mobility of uranium in subsurface sediments.

The influence of calcite on uranium (VI) adsorption was investigated using calcite-containing sandy silt/clay sediment from the U.S. Department of Energy's Hanford site. Uranium (VI) adsorption to the sediment and its size and mineralogical fractions were studied in Na-HCO_3-NO_3 electrolytes (I = 0.05) with variable pH (7.2 to ~10) and uranium (VI) concentrations (10^{-7} to ~10^{-5} M) and with/without saturation to calcite. In the calcite-saturated solutions, uranium (VI) adsorption to the sediment and its fractions consistently increased with increasing pH until pH = 8.4 ± 0.1, and subsequently decreased with increasing pH (Figure 1a). The results contrasted with those in the calcium-free solutions where uranium (VI) adsorption decreased as pH increased above 7.2 (Figure 1b). The uranium (VI) adsorption was almost identical in the calcite-saturated and calcium-free solutions with pH levels above 8.4. Both the speciation calculation (Figure 2a) and laser-induced fluorescence spectroscopic analysis (Figure 2b) revealed that the presence of aqueous calcium in equilibrium with calcite induced the formation of $Ca_2UO_2(CO_3)_{3(aq)}$ that increasingly dominated aqueous uranium (VI) speciation as pH decreased from pH 8.4. Above pH 8.4, the aqueous uranium (VI) speciation was dominated by $UO_2(CO_3)_3^{4-}$ in both calcite-saturated and calcium-free solutions. These results indicated that the species $Ca_2UO_2(CO_3)_{3(aq)}$ competitively decreased uranyl adsorption in the calcite-saturated

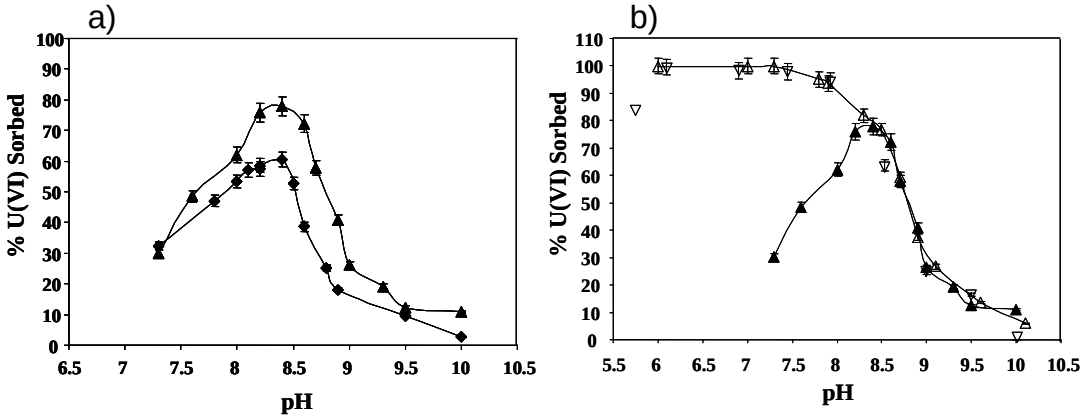

Figure 1. Uranium (VI) adsorption to the Hanford Site clay sediment as a function of pH: a) untreated silt/clay and carbonate-removed silt/clay in calcite-presaturated solutions (▲= carbonate-removed silt/clay and ◆ = untreated silt/clay) and b) carbonate-removed silt/clay with calcite-saturated (▲) and the calcium-free (△) solutions, and both carbonate and iron oxide removed silt/clay in the calcium-free solution (∇) [total uranium (VI)= 1.2×10^{-6} mol/L, solid/solution ratio = 100 g/L, I = 0.05 mol/L ($NaNO_3$), and $P_{CO2} = 10^{-3.5}$ atm].

solutions. Uranium (VI) adsorption to the sediment exhibited additivity in terms of size fraction with the adsorption primarily occurring on the silt/clay fraction below pH 8.5. Above pH 8.5, the sand size fraction also contributed significantly. Removal of iron oxides as a trace component in the sediment (less than 1%) had no effect on uranium (VI) adsorption (Figure 1b). The removal of carbonate minerals, however, increased the uranium (VI) adsorption (Figure 1a), although carbonate was a minor component (approximately 3%) in the sediment. The uranium (VI) adsorption additivity was not observed with respect to the mineralogical component, possibly because of the carbonate-induced blockage of high-affinity uranium (VI) adsorption sites.

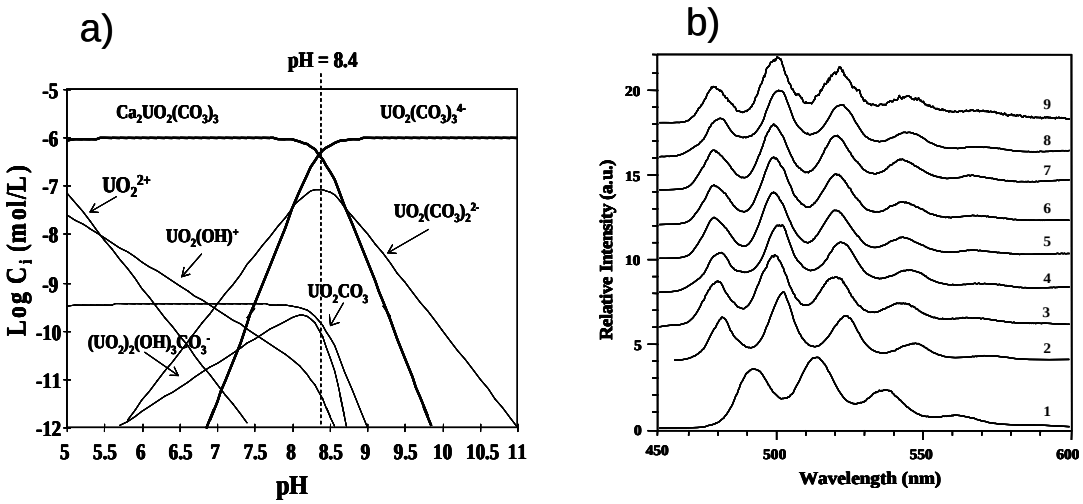

Figure 2. a) Calculated uranium (VI) speciation in the calcite-pre-saturated solution [uranium (VI) = 1.0×10^{-6} mol/L, I = 0.05 mol/L ($NaNO_3$), and $P_{CO2} = 10^{-3.5}$ atm]. b) LHeT fluorescence spectra at a wavelength (λ_{ex}) = 415 nm for 1) standard solution of aqueous $UO_2^{2+}{}_{(aq)}$; 2) standard solution of $Ca_2UO_2(CO_3)_3^{0}{}_{(aq)}$; 3) standard solution of $(UO_2)(CO_3)_3^{4-}{}_{(aq)}$; and samples of the following six sorptions: 4) after contact with untreated silt/clay using calcite pre-saturated solution, [U(VI)] = 0.75×10^{-6} M, pH = 7.3; 5) after contact with untreated silt/clay using calcite pre-saturated solution, [U(VI)] = 0.46×10^{-6} M, pH = 8.3; 6) after contact with untreated silt/clay using initially calcium-free solution, [U(VI)] = 0.92×10^{-6} M, pH = 7.3; 7) after contact with untreated silt/clay using initially calcium-free solution, [U(VI)] = 0.52×10^{-6} M, pH = 8.5; 8) after contact with carbonate-removed silt/clay using initially calcium-free solution, [U(VI)] = 0.78×10^{-6} M, pH = 7.3, and 9) after contact with carbonate-removed silt/clay using calcite-pre-saturated solution, [U(VI)] = 0.25×10^{-6} M, pH = 7.3. For clarity, the spectra were normalized to the same maximum intensities and offset along the vertical axis. The results showed that $Ca_2UO_2(CO_3)_3^{0}{}_{(aq)}$ dominates in solutions in pre-saturated with calcite when pH is less than 8.3, while $(UO_2)(CO_3)_3^{4-}{}_{(aq)}$ dominates in all solutions when pH is greater than 8.3.

A Coupled Model of Electrodynamics and Nonequilibrium Thermodynamics for Describing Ion Diffusion in Porous Media with Fixed Charges and Electrostatic Double Layers

C Liu[(a)]

(a) Pacific Northwest National Laboratory, Richland, Washington

A coupled theory of electrodynamics and nonequilibrium thermodynamics has been developed that may be used to describe ion and charge diffusion in microbial cell membranes, biofilms, and rhizospheres. Understanding these complex biochemical systems will increase the efficiency of wastewater treatment processes that use microbial biofilms to remove pathogens and reduce the amount of organic matter.

A model was formulated to integrate electrodynamics and nonequilibrium thermodynamics for simulation of ion diffusion in porous media that contain fixed charges and electrostatic double layers (Figure 1). The model extends a common multicomponent ion diffusion formulation based on irreversible thermodynamics under a zero ionic charge flux condition, which is only applicable to the regions without fixed charges and electrostatic double layers. A numerical procedure that efficiently solves the coupled differential equations describing electrostatic potential and force and ion concentrations in the model was developed and coded.

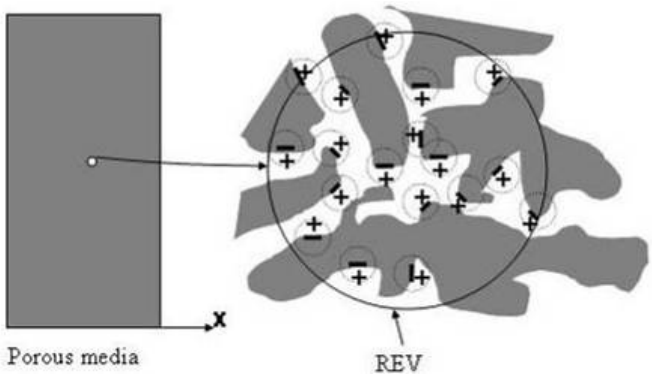

Figure 1. A schematic diagram showing a bulk diffusion region (left) and the structure of a porous medium (right) within a representative elementary volume (REV) that contains frames occupied by solids (shaded area), pores (unshaded area), negative point charges (-), diffusible aqueous cations (+), and electrostatic fields (dotted lines).

Figure 2 shows a model application that considered Mn^{2+} diffusion in negatively charged microbial polysaccharides at the interfaces between plant roots and soil matrix solutions initially in equilibrium with 0.01 mol/dm^3 NaCl without Mn^{2+}. At time zero, 0.0001 mol/dm^3 $MnCl_2$ was introduced into 0.01 mol/dm^3 NaCl bulk solution. Mn^{2+} began to move into the polysaccharide (Figure 2d) in response to the concentration gradient and an electrostatic force induced by the fixed negative charges in the polysaccharides. With Mn^{2+} accumulation, Na^+ moved out of the polysaccharide, but Cl^- changed only slightly with time (Figures 2b and 2c). This phenomenon is a key feature of so-called cation exchange diffusion for ion transport in mucilages at plant and soil interfaces. Because the effect of electrostatic force on divalent Mn^{2+} was larger than monovalent Na^+, Mn^{2+} concentrated more than Na^+ in the polysaccharide relative to their bulk concentrations (Figures 2c and 2d). Increases in cation concentrations at the interface between bulk solution and

polysaccharide were caused by the influence of the electrostatic force that balanced the effect of concentration gradients. The electrostatic force was negative and was strong near the interface between polysaccharide and bulk solution as indicated by the sharp increase of electrostatic potential toward bulk solution (Figure 2a). The accumulation of Mn^{2+} in the polysaccharide decreased the electrostatic potential with time (Figure 2a), which decreased the anion exclusion force and led to the slight increase of Cl^- concentration within the polysaccharide (Figure 2c). The enhanced rate of cation exchange transport in negatively charged polysaccharides was consistent with the microscopic concept of forced diffusion by the local electrical fields along diffusion paths (Figure 1). When the locations of the fixed charges are close enough, cations may be driven from one microscopic electrostatic field to another by the electrostatic force and concentration gradients.

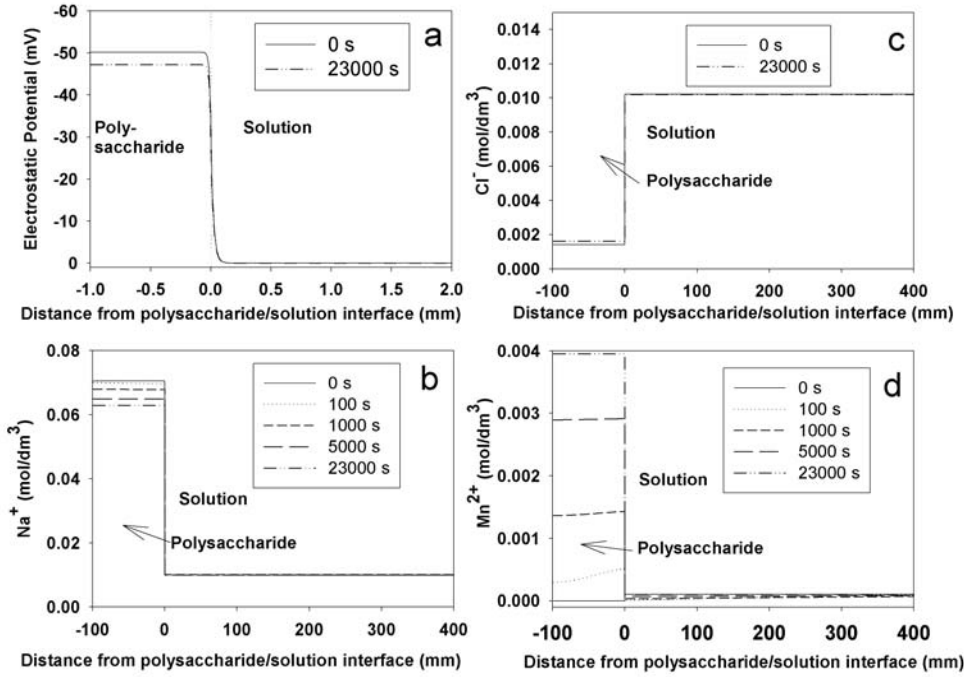

Figure 2. Calculated electrostatic potential a) and diffusion profiles of Na^+ b), Cl^- c), and Cl^- d) in the porous and bulk solution. The porous region was initially in equilibrium with 0.01 mol/dm^3 NaCl bulk solution and diffusion started after introducing 0.0001 mol/dm^3 $MnCl_2$ into the bulk solution. (Ion tracer diffusivity: Na^+ = 1.33, Cl^- = 2.03, and Mn^{2+} = 7.12 x 10^{-10} m^2/s; fixed charge density in the polysaccharide = -6.67 x 10^3 C/dm; tortuosity factor = 14.2; dielectric constant = 78 for bulk solution and = 60 for porous medium; zero ionic flux at x = -100 μm, and continuous mass flux at the interface between the polysaccharide and solution).

Reoxidation of Reduced Uranium with Iron (III)-(Hydr)oxides Under Sulfate-Reducing Conditions

RK Sani,[(a)] BM Peyton,[(a)] AC Dohnalkova,[(b)] and JE Amonette[(b)]
(a) Washington State University, Pullman, Washington
(b) Pacific Northwest National Laboratory, Richland, Washington

Sulfate-reducing bacteria can precipitate uranium in the subsurface and, thus, play a very important role in processes that control stability of uranium to restrict its environmental risk. However, knowledge of these processes under microbial growth conditions is limited. Biogenic removal of uranium from solution can be complicated by reversal of this process under oxidizing conditions.

In cultures of *Desulfovibrio desulfuricans* G20, the effects of iron (III)-(hydr)oxides (hematite, goethite, and ferrihydrite) on microbial reduction and reoxidation of uranium were evaluated under lactate-limited, sulfate-reducing conditions (Figure 1). With lactate present, G20 reduced uranium (VI) in both PIPES and bicarbonate buffer. Once lactate was depleted, however, microbially reduced uranium served as an electron donor to reduce iron (III) present in iron (III)-(hydr)oxides. With the same initial amount of iron (III) (10 mmol/L) for each iron (III)-(hydr)oxide, reoxidation of uranium (IV) was greater with hematite than with goethite or ferrihydrite. As the initial mass loading of hematite increased from 0 to 20 mmol iron (III)/L, the rate and extent of iron (IV) reoxidation increased. Subsequent addition of hematite (15 mmol iron (III)/L) to stationary phase cultures containing microbially reduced uranium (IV) also resulted in rapid reoxidation to uranium (VI). Analysis by uranium L3-edge, x-ray absorption near-edge structure spectroscopy of microbially reduced uranium particles yielded spectra similar to that of natural uraninite.

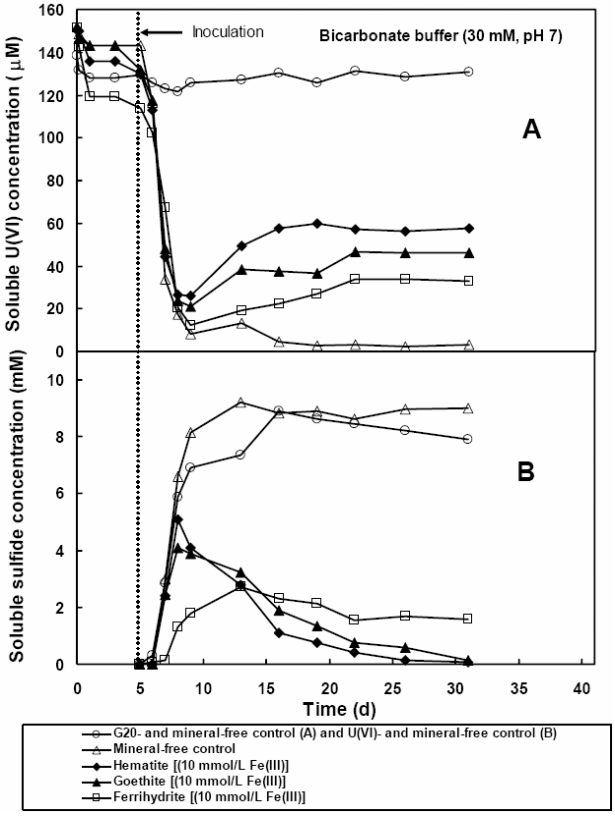

Figure 1. A) Concentration profiles of soluble uranium (VI) during abiotic sorption onto hematite, goethite, ferrihydrite, and quartz in a medium containing bicarbonate buffer, and reduction by *D. desulfuricans* G20; B) concentration profiles of soluble sulfide during growth of *D. desulfuricans* G20.

Observations by high-resolution transmission electron microscopy (Figure 2), selected area electron diffraction, and energy-dispersive x-ray spectroscopic analysis confirmed that precipitated uranium associated with cells was uraninite with particle diameters of 3 to 5 nm. Using the same techniques, iron sulfide precipitates were found to have a variable iron and sulfur stoichiometry and were not associated with cells. The *d*-spacings of randomly selected iron-rich precipitates were most closely related to greigite.

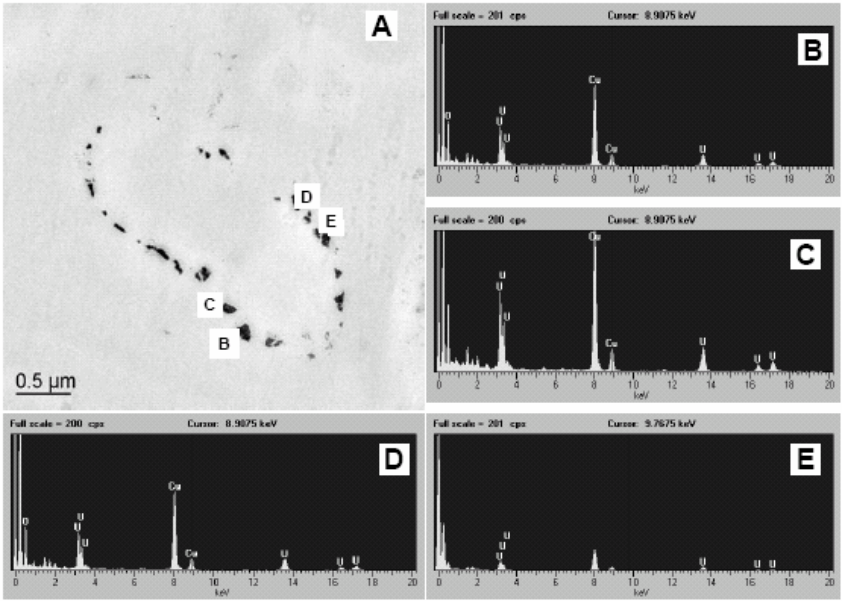

Figure 2. A) Transmission electron microscope image of an unstained thin section of *D. desulfuricans* G20 treated with uranium (VI) and hematite (25 mmol/L) showing an oblique section of a bacterium. In images B, C, D, and E, evident precipitates of biogenic uraninite in cell periplasm were confirmed by energy-dispersive x-ray spectra and selected area diffraction, respectively. The copper background signal originates from the copper grid.

The results provide evidence that *D. desulfuricans* G20 reduced uranium (VI) to form nano-particulate uraninite, which was observed both in the cell periplasm and in the bulk liquid. Further, results indicate that the type and amount of iron (III)-(hydr)oxide present and the type of pH buffer (PIPES or bicarbonate) had significant effects on the rate of uranium (VI) reduction. After depletion of lactate required for microbial uranium (VI) reduction, the rate and extent of uranium (IV) reoxidation were dependent on the type and amount of iron (III)-(hydr)oxide present. These results suggest that application of long-term bio-immobilization of uranuim must consider additional complexity in processes and reactions because sulfate and sulfate-reducing bacteria are commonly found in many uranium-contaminated aquifers.

Synthesis of Colloidal Mn^{2+}: ZnO Quantum Dots and High-Curie-Temperature Ferromagnetic Nanocrystalline Thin Films

NS Norberg,[(a)] KR Kittilstved,[(a)] JE Amonette,[(b)] RK Kukkadapu,[(c)] DA Schwartz,[(a)] and DR Gamelin[(a)]

(a) University of Washington, Seattle, Washington
(b) Pacific Northwest National Laboratory, Richland, Washington
(c) W.R. Wiley Environmental Molecular Sciences Laboratory, Richland, Washington

Magnetic semiconductors can be used to increase data processing speeds and reduce power consumption and equipment dimensions. Reproducible methods for preparing magnetic semiconductors are essential but remain a technical challenge. A direct solution chemical route to create high-quality, manganese-doped zinc oxide quantum dots provides effective control, allowing the preparation of intrinsically ferromagnetic semiconductors.

Diluted magnetic semiconductors (DMSs) are attracting increasing attention in the physics community because of recent predictions and reports of room-temperature ferromagnetism in some of these materials. Ferromagnetic DMSs have been proposed as pivotal components in a new category of spin-based electronics (spintronics) devices that aim to control electron spin currents as well as charge currents to increase data processing speeds, reduce power consumption, reduce hardware dimensions, and possibly introduce new functionalities to semiconductor information processing technologies.

Theoreticians have identified zinc oxide (ZnO) as an excellent candidate host semiconductor for supporting high-Curie-temperature (high-T_C) ferromagnetism when doped with a variety of 3d transition metal ions, particularly Mn^{2+}. Experimentalists have verified these predictions in some cases, with ferromagnetism above room temperature reported for thin films of ZnO doped with Co^{2+}, Co^{2+}/Fe^{2+}, and V^{2+}. These findings remain controversial, however, and several laboratories have claimed to observe ferromagnetism arising only from phase-segregated impurities and not from the DMSs themselves. Reproducible methods for preparing high-T_C ferromagnetic DMSs are essential for their use in spintronics technologies but remains a central technological challenge. Overcoming this challenge will advance our understanding of the fundamental origins of this interesting magnetic behavior.

We have recently reported the direct chemical synthesis of high-quality colloidal Mn^{2+}:ZnO quantum dots and the use of these nanocrystals as solution-phase precursors for the preparation of nanocrystalline thin films by spin-coat processing (Norberg et al. 2004). Synthesis of Mn^{2+}:ZnO nanocrystals in this study was monitored using X- and Q-band electron

paramagnetic resonance, transmission electron, and electronic absorption spectroscopy techniques. The transmission electron microscope images (Figure 1) and the Q-band electron paramagnetic resonance spectroscopy spectra (Figure 2) were obtained using instruments in the W.R. Wiley Environmental Molecular Sciences Laboratory.

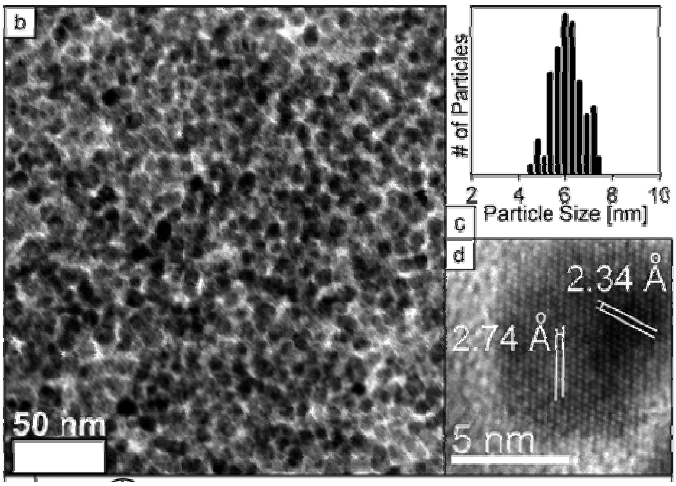

Figure 1. b) Overview transmission electron microscope image of 0.20% Mn^{2+}:ZnO nanocrystals. c) Histogram of 100 crystal diameters (6.1 ± 0.7 nm average diameter). d) High-resolution transmission electron microscope image of a single nanocrystal showing lattice spacings matching those of ZnO.

Robust, high-T_C ferromagnetism in thin films of these nanocrystals prepared by spin-coating with 300 K saturation moments as high as 1.35 μß/Mn^{2+} are nearly an order of magnitude higher than that previously reported. The Mn^{2+}:ZnO ferromagnetism is accompanied by a broad ferromagnetic resonance electron paramagnetic resonance signal that reflects the high multiplicity of the ferromagnetic ground state. The preparation of more complex ferromagnetic semiconductor nanoarchitectures by solution processing methods may therefore be envisioned.

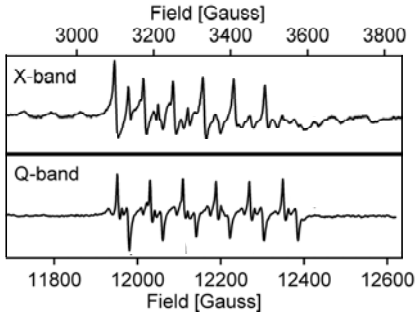

Figure 2. Experimental 300 K X- and Q-band electron paramagnetic resonance spectra of colloidal dodecylamine-capped 0.02% Mn^{2+}:ZnO nanocrystals in toluene.

Reference

Norberg N, K Kittilstved, JE Amonette, RK Kukkadapu, D Schwartz, and D Gamelin. 2004. "Synthesis of Colloidal Mn^{2+}:ZnO Quantum Dots and High-T_c Ferromagnetic Nanocrystalline Thin Films." *Journal of the American Chemical Society* 126(30):9387-9398.

Cell Adhesion of *Shewanella oneidensis* to Iron-Oxide Minerals: Effect of Different Single Crystal Faces

AL Neal,[(a)] TL Cail,[(b)] MF Hochella,[(c)] and KM Rosso[(d)]

(a) University of Georgia, Athens, Georgia
(b) Oak Ridge National Laboratory, Oak Ridge, Tennessee
(c) Virginia Polytechnic Institute and State University, Blacksburg, Virginia
(d) Pacific Northwest National Laboratory, Richland, Washington

The interaction of metal-reducing microorganisms with solid-phase electron acceptors such as iron oxides is among the most complex and important interaction in nature. The attachment of cells to mineral surfaces is a key link in the respiratory action of this class of bacteria. Unraveling the molecular-scale processes occurring at the interface and the underlying genetic apparatus promises new opportunities for understanding and controlling the transport of contaminants in subsurface environments.

Sufficient energy is available from the reduction of ferric iron in both crystalline and noncrystalline iron oxides to support the growth of dissimilatory metal-reducing bacteria for which ferric iron is the dominant electron acceptor. The relative reactivity of various oxide phases in both terrestrial and marine sediments is controlled less by thermodynamic considerations than by the surface area of the respective phases. We have recently demonstrated that when surface area is controlled by presenting cells with single crystal growth faces, differences in cell accumulation of the dissimilatory iron-reducing bacterium *Shewanella oneidensis* MR-1 are observed among three crystal faces that moreover appear consistent with modeled rates of electron transfer from an outer membrane cytochrome (Neal et al. 2003). Thus, fine-scale interactions reflecting the electronic structure of the iron-oxide bulk and near-surface region may also affect biological activity/reduction.

To determine if the strength of cell attachment to mineral surfaces could be related to the propensity for electron transfer into the surface, we measured forces between individual *S. oneidensis* MR-1 cells and a series of flat, single crystal faces of iron oxides. Forces measured between individual cells and three different iron-oxide surfaces upon initial closure of the separation distance are shown in Figure 1. The force data show slight repulsive forces between the approaching cells and the two magnetite surfaces, whereas for hematite, the force is attractive. These observations are consistent with the expected charging behavior of both the oxide and cell surfaces. At

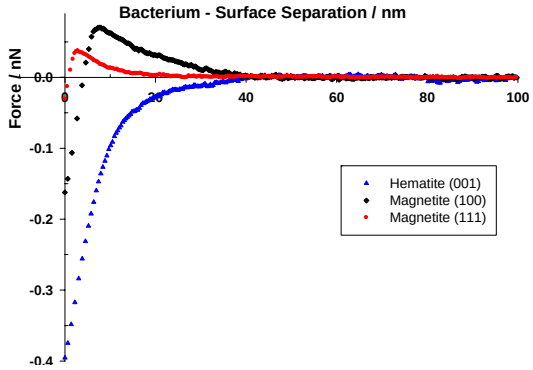

Figure 1. Interaction forces between *S. oneidensis* MR-1 cells and three different iron-oxide single crystal faces upon decreasing the separation distance. Positive forces indicate repulsion, negative forces attraction. All measurements were made at pH 7 in a PIPES-basal medium.

pH 7, the magnetite and cell surfaces are negatively charged, while the hematite surface is positively charged. Thus simple electrostatic arguments are sufficient to explain the approach curves.

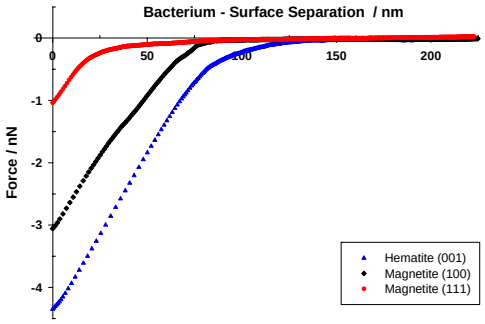

Figure 2. Interaction forces between *S. oneidensis* cells and three different iron oxide single crystal faces upon cell detachment and increasing separation distance. The jump-from-contact force differs significantly among the three surfaces.

However, the forces measured when the cells are retracted after being attached to the surface from between 0.1 and 0.5 seconds ranked in a distinctly different way (Figure 2). Cells were found to bind most strongly to hematite (001), with intermediate strength to magnetite (100), and with the least strength to magnetite (111). Tests with functionalized atomic force microscopy cantilevers devoid of cells showed detachment forces consistent with the differences in the surface charge of the three surfaces. However, when cells are present, the detachment forces are clearly different and are not attributable to electrostatic forces or differences in hydrophobic forces. This finding raises the prospect that some specific adhesive mechanism may influence the measured adhesive forces between iron-reducing bacteria and iron-oxide surfaces.

This series in adhesive force is consistent with previous observations of cell accumulation at the mineral faces where maximum cell densities are observed on hematite (001) (Neal et al. 2003). Also, relatively more daughter cells are released from the two magnetite surfaces compared to hematite. This compelling evidence suggests that some as yet unidentified property of the mineral surface can influence not only adhesion/attachment but also growth and detachment of *S. oneidensis* cells. Predictions of the rate of electron transfer from OmcA, an outer membrane c-type cytochrome, to the respective mineral faces can be systematically related to the observations of adhesive force. Those surfaces to which electron transfer is likely to be fastest (i.e., hematite [001]) support the greatest force of adhesion and the greatest cell density. Surfaces to which electron transfer is predicted to be slowest (i.e., magnetite [111]) support the least adhesive force. In both cases magnetite (100) is intermediate.

Our study is the first to demonstrate that the adhesion forces measured at the three faces reflect more the expected rate of electron transfer from outer membrane-associated cytochromes to the mineral surfaces and less the assumed surface charge.

Reference

Neal AL, KM Rosso, YA Gorby, GG Geesey, and B Little. 2003. "The Effects of Surface Structure on Dissimilatory Reduction of Iron Oxides by *Shewanella oneidensis*." *Geochimica Cosmochimica Acta* 67(23):4489-4503.

Reoxidation of Bioreduced Uranium Under Reducing Conditions

J Wan,[(a)] TK Tokunaga,[(a)] J Larsen,[(a)] Z Zheng,[(a)] E Brodie,[(b)] Z Wang,[(c)] D Herman,[(b)] TC Hazen,[(a)] MK Firestone,[(b)] and SR Sutton[(d)]

(a) Lawrence Berkeley National Laboratory, Berkeley, California
(b) University of California, Berkeley, California
(c) Pacific Northwest National Laboratory, Richland, Washington
(d) University of Chicago, Chicago, Illinois

The mining and processing of uranium for use in nuclear weapons and fuel have left thousands of sites with toxic levels of this actinide in soil and groundwater. An emerging strategy for remediating such environments involves using organic carbon to promote microbially mediated reduction and precipitation of insoluble uranium minerals. However, recent results have shown that these processes are not sustainable in carbonated, neutral-to-alkaline soils and groundwater.

The mobility of uranium depends strongly on its oxidation state, with uranium (IV) species being much less soluble than uranium (VI) species under most environmental conditions. Based on findings that a number of iron- and sulfur-reducing bacteria also reduce uranium (VI) enzymatically as well as indirectly, a strategy under development for remediating uranium-contaminated soil and groundwater is based on promoting reductive precipitation of low solubility uranium (IV) minerals. Emerging techniques rely on injecting organic carbon into contaminated sediments to stimulate direct or indirect microbial uranium (VI) reduction to uranium (IV) solids. However, accounts of organic-carbon-stimulated bacterial uranium reduction have only reported results for short times after conversion of uranium (VI) to uranium (IV). Although dissolved oxygen, nitrate, and denitrification products have been shown to oxidize uranium, such results are expected from inspection of the redox ladder. When unperturbed by influxes of highly oxidizing terminal electron acceptors, uranium (IV) is commonly assumed to be stable in reducing sediments. This study examines the stability of bioreduced uranium under such conditions.

The experiment was conducted using soils obtained from Oak Ridge National Laboratory that had been heavily contaminated from past uranium waste disposal (uranium concentration of 206 mg/kg). The soils were packed into columns (200-mm length, 32-mm inner diameter), and permeated with 10.7-mM sodium-lactate solution (32-mM organic carbon, pH 7.2) to stimulate uranium bioreduction by the native microbial community. The solution was supplied at a pore fluid velocity of 20 mm/d for 215 days, after which the pore fluid velocity was decreased to 10 mm/d. Concentrations of uranium, organic carbon, inorganic carbon, methane, carbon dioxide, iron, manganese, calcium, and pH were determined in effluents. Redox potentials were measured within columns with platinum electrodes, and also calculated based on ratios of methane and carbon dioxide concentrations. Oxidation states of uranium within the soil were measured within columns at days 117 and 356 by synchrotron micro-x-ray absorption, near-edge structure (μ-XANES) spectroscopy, while uranium (VI) speciation in the effluents was determined by liquid-helium temperature, time-resolved, laser-induced fluorescence spectroscopy (Figure 1).

Under constant reducing conditions, the concentration of uranium in the effluent was initially very high, typically exceeding 10 μM, which is indicative of the initial oxidizing condition. The nearly complete conversion of organic carbon to bicarbonate and methane along with the results of bioassay confirmed the presence of active microbial populations in the sediment. Direct analyses of the soils by μ-XANES spectroscopy showed variable, but generally reduced conditions, with 87% (±26%) of the uranium occurring as uranium (IV) on day 117. After this early stage of lactate infusion, uranium concentrations declined by three orders of magnitude to less than 30 nM by day 100 even though the cumulative uranium removal in effluents at this time still left 98.8% of the initial uranium in the soil. However, upon further permeation with the lactate solution and sustained reducing conditions, uranium concentrations in effluents increased thirtyfold, returning to over 1 μM at days 120 to 200. Thereafter, the uranium concentration remained fairly constant.

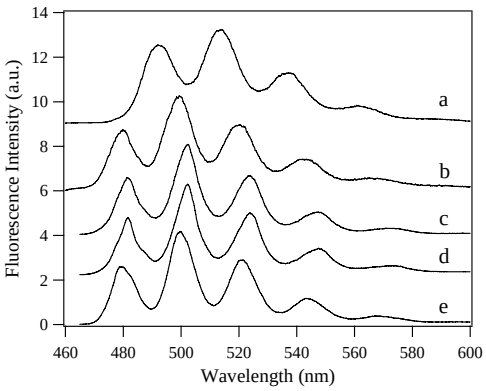

Figure 1. Fluorescence spectra of aqueous uranyl complexes at 6 K: λ_{ex} = 415 nm. The solution conditions were a) $[UO_2^{2+}] = 5 \times 10^{-5}$ M in nitric acid, pH 2.5; b) $[UO_2^{2+}] = 5 \times 10^{-6}$ M in 0.034 M Na_2CO_3 solution, $P(CO_2) = 1$ atm, pH = 10.6; c) $[UO_2^{2+}] = 1.17 \times 10^{-4}$ M, $[NaHCO_3] = 7 \times 10^{-8}$ M, $[Ca^{2+}] = 5 \times 10^{-8}$ M, $P(CO_2) = 10^{-3.5}$ atm, pH = 7.4; d) effluent C1-5, collected at the time before reduction occurred; e) effluent C1-223, collected at the steady-state of reoxidation stage. For clarity, the spectra were normalized to the same maximum intensities and offset along the vertical axis.

A similar trend was observed for total inorganic carbon in effluents, with a steady-state concentration of 12.7 mM, primarily as HCO_3^-. At the same time the soil uranium (IV) content declined to 58% (±22%) of the total uranium when measured on day 356 with 97.6% of the original uranium still in the soil. The cryogenic fluorescence spectra of effluent samples shows close resemblance to those of $Ca_2UO_2(CO_3)_3$ and $UO_2(CO_3)_3^{4-}$ complexes (Figure 1), indicating their presence. These fluorescence spectra along with measured redox potentials (E_h) suggest that the reoxidation of U(IV) to U(VI) favors the formation of the aqueous complexes $Ca_2UO_2(CO_3)_3$ and $UO_2(CO_3)_3^{4-}$ in the presence of appreciable concentrations of Ca^{2+} (resulting from dissolution of calcite) and elevated carbonate concentrations (due to microbial activities).

Cryogenic Laser-Induced Uranium (VI) Fluorescence Studies of a Uranium (VI) Substituted Natural Calcite: Implications to Uranium (VI) Speciation in Contaminated Sediments

Z Wang,[(a)] JM Zachara,[(a)] JP McKinley,[(a)] SC Smith,[(a)] and SM Heald[(b)]
(a) Pacific Northwest National Laboratory, Richland, Washington
(b) Argonne National Laboratory, Argonne, Illinois

Chemical speciation and imaging techniques were used to examine uranium-contaminated subsurface sediments from the U.S. Department of Energy's Hanford Site in southeastern Washington. Measurements implied that waste uranium, which had been present for a long time beneath the sampled disposal pond, had precipitated from the waste as carbonate salts. These results have major implications for the solubility and fate of contaminants.

The interaction of uranium with carbonate minerals, particularly the calcium carbonate polymorphs calcite and aragonite, has an important bearing on the mobility of contaminant uranium in near-surface environments. In the near surface, uranium is prevalently hexavalent, and occurs as the uranyl ion, UO_2^{2+}, which forms strong carbonato complexes. The association of uranyl with carbonate minerals, either sorbed on the mineral surface or incorporated in the mineral structure through co-precipitation, could have a controlling influence on its mobility. In addition, the relative solubility and stability of carbonate minerals containing uranyl could determine its long-term availability for remobilization, and co-precipitation of uranyl with carbonate minerals occurs with complex variations. In this study, we used time-resolved, laser-induced fluorescence spectroscopy (TRLFS) to examine the crystallographic environment of uranyl in sediments from a uranyl-bearing infiltration pond with uranium concentrations ranging from 360 to 3300 ppm at the U.S. Department of Energy's Hanford Site in southeastern Washington. We also contrast these highly disturbed environmental results with results from a previously studied natural, uranyl-bearing calcite (NUC). The NUC specimen (360 mg U/kg) originally retrieved from a 13,700-year-old speleothem deposit in the Vinschgau Valley of northern Italy was provided by Argonne National Laboratory. X-ray diffraction analysis indicated that the sample was more than 99.8% pure calcite.

Composite time-resolved fluorescence images (TRLFISM) at a series of delay times and gate widths were acquired from the NUC, over an area of approximately 7 mm by stepping the X-Y translation stage. The distribution of fluorescence (Figure 1) showed a relatively small dynamic

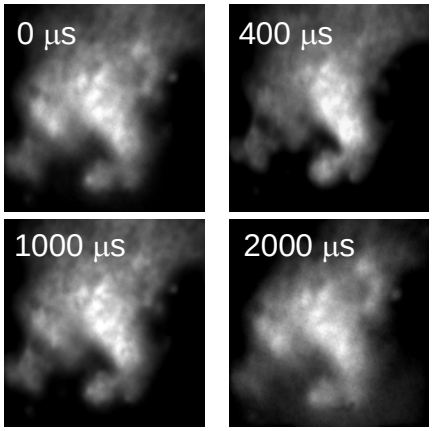

Figure 1. TRLFISM of the NUC sample at different delay times. λ_{ex} = 415 nm.

range, indicating that uranium was distributed more or less uniformly with the sample. Fluorescence was also relatively uniform across measurements at different delay times (Figure 1), indicating that individual contributors of the fluorescence signal were uniformly distributed. Time-resolved fluorescence spectra recorded at multiple delay times between 0 and 4 ms for bulk crystals showed that at the same delay times, the spectral characteristics were similar for spectra obtained on the bulk (TRLFS) and microscopic (TRLFISM) systems, regardless of the spatial location of the area examined or its relative intensity, which was presumably proportional to the relative concentration of uranium within the crystal. However, the fluorescence spectra showed significant, systematic changes as a function of the delay time. At shorter delay times, the spectra were less resolved with a spectral maximum located at approximately 513 nm (Figure 2). The spectral resolution increased as the delay time increased, and well-resolved spectra were observed after a delay of about 2 ms.

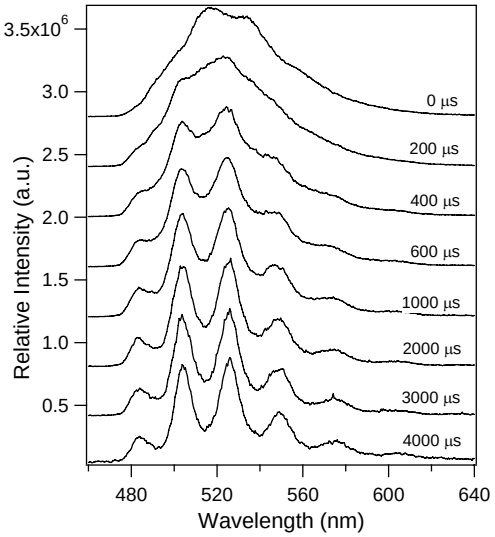

Figure 2. Cryogenic TRLFS spectra of a natural uranium-rich calcite at a series of delay times. λ_{ex} = 415 nm. The maximum intensities were normalized for comparison and the spectra were offset along the Y-axis.

By assigning the long delay spectrum to a single component (trace B, Figure 3), all of the spectra were definable by linear combinations of two unique spectral components, which were designated A and B (Figure 3). The spectrum of the longer-lived uranyl species (B) in NUC was almost identical to that of uranyl incorporated into aragonite, while the spectrum of the shorter-lived species (A) was similar to that of uranyl incorporated into synthetic calcite. Comparison of our long-lived spectra from the NUC with other results suggested that it was similar to the aqueous tricarbonate species.

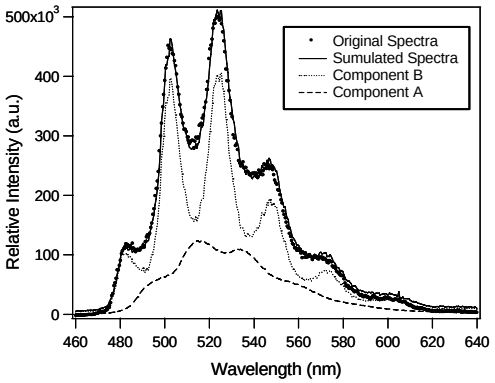

Figure 3. Deconvolution of the LHeT time-resolved fluorescence spectra of the uranium-rich natural calcite at a delay time of 1 ms into two unique spectral components: A and B.

Both the sediment samples were examined using TRLFISM and TRLFS with similar procedures applied for the NUC. TRLFISM at a series of delay times indicated that long-lived fluorescence was present. The distribution of fluorescence and the relative fluorescence intensity varied spatially. For some large clasts, fluorescence varied significantly within the clast, and for a given set of fluorescent clasts, the relative fluorescence intensities varied as a function of delay. These observations were clear indications of the presence of multiple uranyl species and of compositional heterogeneity.

The evolution of TRLFS spectra of sediment NP4-1 (Figure 4) displayed a similar pattern to that of the NUC (Figure 2), and in fact, the spectral features of the NP4-1 at delay times longer than approximately 600 μs were nearly identical to that of the NUC. The TRLFS spectra of NP4-1 sediment were analyzed following the same procedures for the spectral simulation of the NUC. All of the spectra of NP4-1 could be simulated by the linear combination of two spectral components, one with lower spectral resolution and a spectral maximum at approximately 517 nm and another with high spectral resolution and a maximum at 501 nm. The fluorescence decay curves for sediment NP4-1 could also be well fitted by the biexponential-function-resulting fluorescence lifetimes of 422 μs and 92 μs, respectively.

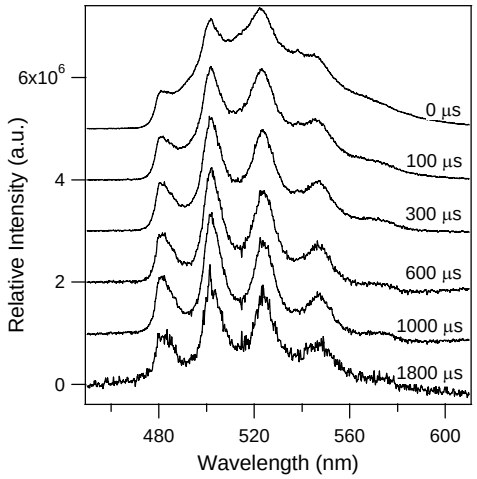

Figure 4. Cryogenic TRLFS spectra of NP4-1 sediments at a series of delay times. λ_{ex} = 415 nm. Gate width = 100 μs. For comparison, the maximum intensities of the spectra were normalized and offset along the Y-axis.

Comparisons of the fluorescence spectra and lifetimes of the uranyl species in NP4-1 with those of the NUC suggested that the same type of uranyl species were present in both samples. The spectral features of the component B in both samples were almost identical, and those for component A were also very close, despite a small shift of the spectral origin towards longer wavelength. Considering the similar fluorescence lifetimes for uranyl species B in NP4-1 and NUC, the difference in delay times at which species B became dominant (600 μs for NP4-1; 2 ms for NUC) indicated that the relative concentration of this 'aragonite' component was much higher in NP4-1 than in the NUC.

Carbonate minerals are among the most common secondary minerals formed in nature, and dissolved carbonate is a common component of waste solutions containing uranium. The presence of similar uranyl species in the NUC and the Hanford Site sediments implied that the reaction of uranyl with calcite, either through surface precipitation or co-precipitation, facilitated uranium (VI) sorption in the sediments.

Development of a Mixed Solvent-electrolyte Thermodynamic Model for Calculating the Binding of Actinides to Microbial Membranes

AR Felmy,[(a)] SB Clark,[(b)] and O Qafoku[(a)]
(a) Pacific Northwest National Laboratory, Richland, Washington
(b) Washington State University, Pullman, Washington

Microbial surfaces can take up high concentrations of metal, lanthanide, and actinide species through biosorption, reduction, or precipitation. Developing realistic thermodynamic models for metal binding on microbial surfaces will aid in understanding the different binding mechanisms of the bacteria, leading to the advancement of effective bioremediation techniques.

Microbial surfaces are known to take up high concentrations of metal, lanthanide, and actinide species through biosorption, reduction, or precipitation. The surfaces of gram-negative bacteria (the most environmentally important microorganisms) are principally composed of an outer layer of lipopolysaccharides (LPSs), phospholipids, and lipoproteins. The outer layer of LPSs, in particular, has been implicated in the attachment of gram-negative bacteria to mineral surfaces and in the binding of metals and actinide species. These LPS layers are composed of a core lipid; an inner core containing phosphate, carboxylate, and amine groups; and an outer O-antigen chain consisting mostly of hydrophobic sugars (depending upon the specific genomic type). Each individual LPS contains highly variable phosphate and carboxylate linkages. The different LPS chains also cross-link in metal binding reactions with multiple LPS chains binding a single metal ion (Lins and Straatsma 2001), resulting in very complex metal-ligand structures that cannot be reproduced in homogeneous aqueous solution.

A key factor in developing thermodynamic models for metal binding in microbial surfaces is the effect of a variable solvating environment. The solvating environment varies in the membrane from regions in the membrane core that are completely hydrophobic through a partially solvated region in the outer membrane to complete solvation in the contacting aqueous solution (Figure 1).

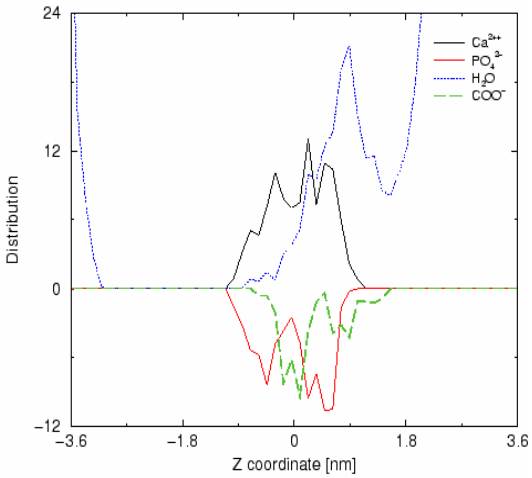

Figure 1. Calculated distribution of calcium, phosphate, carboxylate, and water in the LPS membrane of gram-negative bacteria (Lins and Straatsma 2001).

Implementing more realistic thermodynamic models of the microbial surface requires thinking about the microbe surface not as a flat plane of adsorption but as a variably solvating structure of finite size capable of absorbing metal ions in different microstructures or microenvironments. This new formulation must therefore account for variations in metal

ion solvation, changes in ionic strength with variations in water content, and the ability to determine the free energies of complex metal-ligand structures, which owing to the variable state of solvation may lack analogs from studies in pure water as the solvent. These issues suggest the use of thermodynamic formalisms based more on mixed-solvent-electrolyte approaches than on simple surface-adsorption modeling. Fortunately, a great deal of progress has taken place in the development of mixed-solvent-electrolyte models, including the ability to take into account variations in the dielectric constants for solvent-electrolyte mixtures (Wang and Anderko 2001) and to include complex chemical species within the modeling framework (Wang et al. 2002). In addition, these mixed-solvent-electrolyte models have been found to be capable of modeling the aqueous thermodynamic of the mixed solvents to the pure solvent limits and to exceptionally high ionic strength (i.e., the fused salt limit).

We initiated studies on the incorporation of the mixed-solvent-electrolyte model algorithms into our current thermodynamic codes and are developing the necessary experimental protocol for treating mixed solvent electrolyte systems.

The incorporation of the mixed-solvent-electrolyte model requires inclusion of an algorithm for computing the dielectric constant as a function of solution composition (Wang and Anderko 2001), as well as algorithms for the long-, short-, and middle-range contributions to the activity coefficient expressions (Wang et al. 2002). In addition, to solve the chemical equilibrium problem, the derivatives of these expressions with respect to mole number must also be included in the Hessian matrix of our computer code geochemical modeling code (GMIN) (Felmy 1995). In recent work, the algorithms for the dielectric constant and the long-range term in the activity coefficient expression were included in our thermodynamic models. Future work will include both the short- and middle-range terms in the activity coefficient expressions.

Experimentally, a final protocol was developed for determining the pH for mixed solvent systems. Time-resolved laser fluorescence spectroscopy was used for determining the changes in ion solvation as a function of water content in methanol-water systems, and the solubility of $Eu(OH)_3$ was measured as a function of ionic strength in methanol-water systems. Figure 2 presents some of our initial results for the solubility of $Eu(OH)_3$ in methanol-water systems.

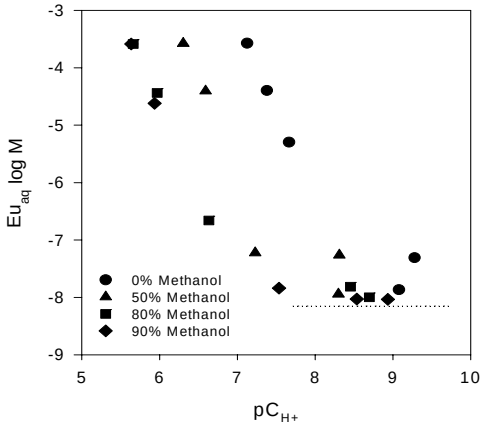

Figure 2. The solubility of $Eu(OH)_3$ in methanol-water systems at room temperature.

These results show that the water content and the solvating environment (the solubility) can vary by almost three orders of magnitude. Such large differences in solubility, related to ionic hydration and activity relations, can greatly alter the calculation of ionic activities in microbial membranes and influence the precipitation of solids at microbial

surfaces. Future experimental studies will complete the $Eu(OH)_3$ solubilities in NaCl-methanol-water systems and extend the results to include ligands of possible biological importance.

References

Felmy AR. 1995. "GMIN: A Computerized Chemical Equilibrium Model Based Upon a Constrained Minimization of the Gibbs Free Energy." *Chemical Equilibrium and Reaction Models*, ed. by RH Loeppert et al., chapter 18, pp. 337-407, Soil Science Society of America, Madison, Wisconsin.

Lins RD and TP Straatsma. 2001. "Computer Simulation of the Rough Lipopolysaccharide Membrane of *Pseudomonas aeruginosa*." *Biophysical Journal* 81(2):1037-1046.

Wang PM and A Anderko. 2001. "Computation of Dielectric Constants for Solvent Mixtures and Electrolyte Solutions." *Fluid Phase Equilibria* 186(1-2):103-122.

Wang PM, A Anderko, and RD Young. 2002. "A Speciation-Based Model for Mixed-Solvent Electrolyte Systems." *Fluid Phase Equilibria* 203(1-2):141-176.

Ferrous Hydroxy Carbonate is a Stable Transformation Product of Biogenic Magnetite

RK Kukkadapu,[(a)] JM Zachara,[(b)] JK Fredrickson,[(b)] DW Kennedy,[(b)] AC Dohnalkova,[(b)] and DE McCready[(a)]

(a) W.R. Wiley Environmental Molecular Sciences Laboratory, Richland, Washington
(b) Pacific Northwest National Laboratory, Richland, Washington

The bacterial transformation of a poorly crystalline iron oxide formed a surprisingly reactive nanometer-size form of magnetite that reacted with naturally occurring carbonate to form a ferrous hydroxy carbonate, a mineral never before seen as a product of bacterial activity. The biogeochemical cycle of microbe-mineral interactions is vital to modeling and enabling bioremediation processes.

Dissimilatory iron-reducing bacteria (DIRB) catalyzes the reduction of iron (III) to iron (II) in soils, sediments, and subsurface sediments. A variety of biomineraliation products result from the interaction of DIRB with iron (III)-oxides, including fine-grained magneite under specific conditions (Kukkadapu et al. 2004). Although fine-grained magnetite is a frequently observed laboratory transformation product of iron (III) oxides by DIRB, there are few reports of biogenic, fine-grained magnetite in soils, sediments, and subsurface materials that have experienced *in situ* dissimilatory iron reduction. The reasons for this absence in natural settings are unknown. Perhaps magnetite is unstable under iron-reducing conditions because of its small size or other properties resulting from biosynthesis.

Recently, we noted that the iron (II)/iron-total ratio of a fine-grained biogenic magnetite (approximately 10 nm) produced by DIRB (Kukkadapu et al. 2004) was in excess (0.5 to 0.6) of stoichiometric magnetite (0.33). Iron (II)-excess magnetites or cation-excess magnetite of varying iron (II)/iron-total ratio (0.4 to 0.6) have been reported in the catalyst research area. Combustion-excess magnetites promoted complete reduction of carbon dioxide to carbon. The high reactivity of cation-excess magnetites for oxidized carbon compounds compared to stoichiometric magnetites, and its lack of persistence in natural settings where bacterial reduction has occurred, may result from its excess iron (II) or small particle size.

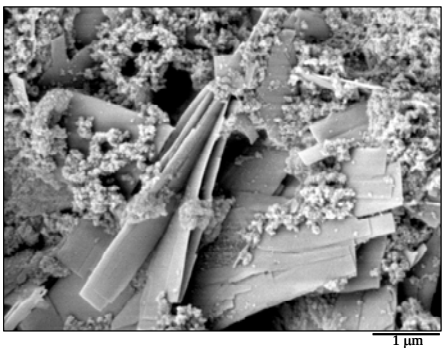

Figure 1. Transmission electron microscope image of a 22-month sample showing ferrous hydroxyl carbonate (micron-size plates) and ground mass of magnetite.

In this study we followed the stability of a fine-grained biogenic cation-excess magnetite in the presence of microbial oxidation products of lactate (carbonate and acetate). The initially bioproduced cation-excess magnetite slowly transformed (partially) with aging to ferrous hydroxy carbonate observed in transmission electron microscopy (Figure 1) and x-ray diffraction (Figure 2). The x-ray diffraction peaks

and morphology (micron-size platy crystallites mixed with cation-excess magnetite) matched well with ferrous hydroxy carbonate (Erdös and Altorfer 1976). Ferrous hydroxy carbonate grew at the expense of cation-excess magnetite. Approximately 50% of the cation-excess magnetite was transformed to ferrous hydroxy carbonate during a 22–month period.

Consistent with x-ray diffraction and microscopy, a doublet due to an iron (II) mineral phase was observed in Mössbauer spectra (not shown). Reaction with carbonate and recrystallization to eliminate iron (III), or to enrich in the residual cation-excess magnetite, apparently led to the ferrous hydroxy carbonate structure. Combined Mössbauer and chemical measurements indicated a general decrease in the iron (II)/iron-total ratio of the residual cation-excess magnetite (to approximately 0.45) during the initial stages of ferrous hydroxy carbonate formation (21 to 28 days), implying recrystallization of a portion of the cation-excess magnetite.

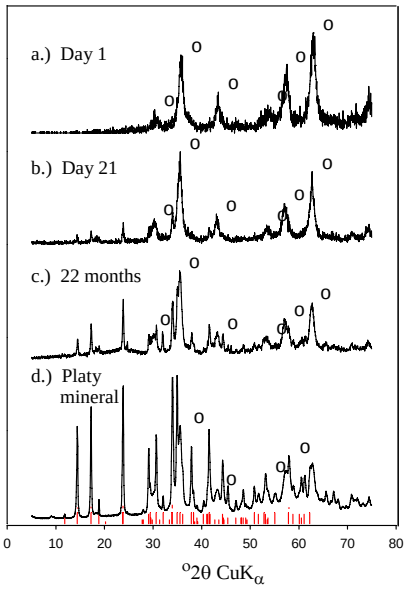

Figure 2. X-ray diffractograms: Transformation of cation-excess magnetite to ferrous hydroxy carbonate with time. Magnetite peaks are labeled by "o." Diffraction peaks for ferrous hydroxy carbonate are shown in red.

Our findings indicated that ferrous hydroxy carbonate can result from remineralization of fine-grained, biogenic cation-excess magnetite from DIRB under anoxic conditions. The apparent susceptibility of fine-grained biogenic cation-excess magnetite to transform to ferrous hydroxy carbonate may explain why the former phase is not more commonly observed in the sediments that have experienced iron (III) reduction. Whether biogenic cation-excess magnetite instability is promoted by its small, nanometer crystallite size or excess iron (II) remains undetermined. Presumptive evidence suggests that excess iron (II) is important. Cation-excess magnetites are likely, however, to be unique products of topotactic magnetite formation by DIRB. In contrast, single-domain magnetite crystallites resulting from magnetotactic bacteria are larger (approximately 50 nm) and stoichiometric in composition, and they appear more stable because they can persist for long periods as microfossils. The apparent instability of cation-excess magnetite to ferrous hydroxy carbonate has important implications for magnetic stratigraphy, as our results show that a certain sequence of microbially mediated reactions may rapidly transform fine-grained magnetite from DIRB to a non-magnetic iron (II) compound.

References

Erdös VE and H Altorfer. 1976. "Ein dem Malachit ähnliches basisches Eisenkarbonat als Korrosionsprodukt von Stahl." *Werkstoffe und Korrosion* 27(5):304-312.

Kukkadapu RK, JM Zachara, JK Fredrickson, and DW Kennedy. 2004. "Biotransformation of 2-Line Silica-Ferrihydrite by a Dissimilatory Fe(II)-Reducing Bacterium: Formation of Carbonate Green Rust in the Presence of Phosphate." *Geochimica Cosmochimica Acta* 68(13):2799-2814.

Molecular Templating for Highly Selective Detection of Relatively Small Molecules

RS Addleman,[(a)] GE Fryxell,[(a)] JT Bays,[(b)] AE Bjerke,[(b)] and Z Wang[(a)]
(a) Pacific Northwest National Laboratory, Richland, Washington
(b) United States Military Academy, West Point, New York

Interest in highly selective, robust, and reliable methods of detecting small molecules from among many interfering species has burgeoned in the past two years with increasing concern about the early detection of chemical agents or unexploded ordinance. Ideally, the presence of specific compounds would be detected at trace levels with absolute accuracy to minimize exposure and reduce the potential for false positive responses.

Previous and ongoing work has focused on the creation and functionalization of a high-surface-area silica layer (mesoporous silica) bound to a silicon substrate. Mesoporous materials with a surface area of approximately 1000 m^2/g covered with a variety of monolayer coatings are now readily available. The self-assembled monolayer consists of functional groups tethered to the silicon surface to form the self-assembled monolayer on a mesoporous support. Functional groups are chosen for their ability to directly bind with either a molecule of interest or to coordinate to lanthanide ions to which a molecule of interest may bind. The molecule of interest may then be templated to give lock-and-key selectivity. Analyte detection may then be accomplished through a variety of methods.

In our most recent studies of these materials, MCM-41, a granular mesoporous silicate, was first functionalized with 1,10 phenanthroline (1,10-phen) because we expected that 1,10-phen would bind with europium ions. Emission and excitation fluorescence spectra were collected for the bare mesoporous substrate and minimal levels of fluorescence were observed in both configurations. Fluorescence spectra were also taken of the 1,10-phen functionalized mesoporous surface, and several broad spectral features appeared that were attributable to the added functional group. Europium then was bound to the 1,10-phen by soaking the substrate in a dilute acidified $EuCl_3$ solution. The substrate was washed, and then fluorescence spectra were obtained. The resulting fluorescence spectrum indicated that europium had bonded to the surface of the 1,10 phen functionalized MCM-41 material (Figure 1).

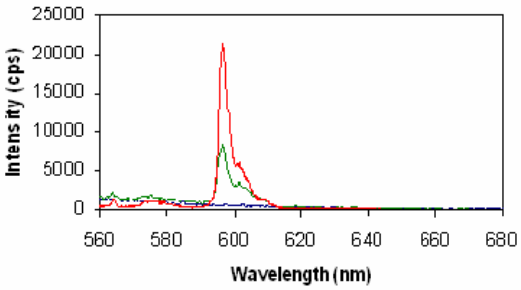

Figure 1. Variation in emission spectra of mesoporous silicate nanoparticles with respect to increasing functionalization. The least intense spectrum (blue) is for 1,10-phenanthroline tethered to a mesoporous layer on MCM-41. The medium intensity spectrum (green) results when Eu^{3+} is bound to the 1,10-phenanthroline used to obtain the first spectrum. The highest intensity spectrum (red) results when TTA is subsequently bound to the Eu^{3+}.

To further enhance the emission signal, thionyltrifluoroacetoacetonate (TTA) was bound to the europium. Samples of the europium-doped 1,10-phen functionalized MCM-41 were

exposed to an aqueous TTA solution. After the substrate was thoroughly washed, the fluorescence emission attributable to the europium complexed with the 1,10-phen on the substrate was significantly enhanced along with absorption at the excitation wavelength. Figure 1 shows the enhancing effect of the addition of TTA to a europium-doped 1,10-phen functionalized MCM-41 surface. In addition to the use of TTA, the effect of several other compounds on the europium fluorescence signal were also studied using fluorescence in both excitation and emission modes.

The successes of this work demonstrate progress towards using monolayers on mesoporous surfaces as detectors for specific compounds of interest. The work also demonstrated the challenge associated with enhancing the fluorescence of certain molecules under a variety of conditions. We expect to continue our investigation of the effectiveness of these sequentially functionalized substrates for obtaining fluorescence enhancement by modifying both the methods of application and solution conditions to ascertain the effect of the chemical environment on this method of detection.

User Projects

Deinococcus radiodurans for Bioremediation: Non-Nuclear

HM Kostandarithes, JK Fredrickson
Pacific Northwest National Laboratory, Richland, Washington

Laboratory Studies of Phytoremediation and Apatite Sequestration

JL Phillips, JE Szecsody
Pacific Northwest National Laboratory, Richland, Washington

Quantum Cascade Laser Photoacoustic Sensor

JE Amonette
Pacific Northwest National Laboratory, Richland, Washington
SE Bialkowski
Utah State University, Logan, Utah

Formation of Iron (II) Secondary Minerals After Iron (III) Bioreduction in Humid Tropical Forest Soils

T Peretyazhko, G Sposito
University of California, Berkeley, Berkeley, California

Mössbauer Analysis for Goethite Reacted with Iron (II) and Membrane Fraction of *Shewanella oneidensis*

J Jang
Pennsylvania State University, University Park, Pennsylvania

Geochemical Testing and Model Development: Residual Tank Waste

KJ Cantrell, WJ Deutsch
Pacific Northwest National Laboratory, Richland, Washington

Novel Nanoporous Getters to Immobilize Technitium-99 at the Yucca Mountain Repository

AR Felmy, OS Qafoku
Pacific Northwest National Laboratory, Richland, Washington

Environmental Sensing, Metabolic Response, Regulatory Network

JK Fredrickson, DW Kennedy
Pacific Northwest National Laboratory, Richland, Washington

Proteomics of Bioenergetics

J Scholten, DW Kennedy
Pacific Northwest National Laboratory, Richland, Washington

Demonstration of the Capability of Mobility-Controlled Flooding Technology to Overcome Heterogeneity-Induced Bypassing in Subsurface Remediation
L Zhong
Pacific Northwest National Laboratory, Richland, Washington

Simulating Mineral Interfaces
JH Weare, SA Bogatko
University of California, San Diego, La Jolla, California

Electronic Structure Determination on Mineral Surfaces
KM Rosso
Pacific Northwest National Laboratory, Richland, Washington
U Becker
University of Michigan, Ann Arbor, Michigan

Use of Near-Field Scanning Optical Microscopy for Characterization of Surface Properties and Processes Affecting Contaminant Transport in the Vadose Zone
JG Hering
California Institute of Technology, Pasadena, California

Developing a Parallel Blochl Code
M Valiev
W.R. Wiley Environmental Molecular Sciences Laboratory, Richland, Washington

Metal and Radionuclide Bioremediation by Starvation Promoter-Driven Combinatorial Bacteria
AC Matin
Stanford University, Stanford, California

Enhancing Carbon Sequestration in Terrestrial Ecosystems: Linking Carbon and Nitrogen Cycling in Soils
VL Bailey, SJ Fansler, DW Kennedy
Pacific Northwest National Laboratory, Richland, Washington

Use of SEM/TEM for Analysis of MR-1 Biofilms Grown for EMSL NMR Microscopy
BD Wood
Oregon State University, Corvallis, Oregon

Atomic Force Microscope Characterization of Self-Assembled Heterogenite Particles
RL Penn
University of Minnesota, Minneapolis, Minnesota

Effects of Impermeable-Zone Diffusion on Continuous and Intermittent Pump-and-Treat Remediation at Dover Air Force Base: Model Simulations and Field Results

W Ball
Johns Hopkins University, Baltimore, Maryland

Electron Paramagnetic Resonance Studies of Copper Sorption on Clay Minerals

DG Strawn
University of Idaho, Moscow, Idaho

Quantitative Measurements in Scattering Media: Path Length Determination of Short Wavelength Near Infrared Light in Fish Tissue

AG Cavinato, SP Nord, RA Tache
Eastern Oregon University, La Grande, Oregon
M Lin, B Rasco
Washington State University, Pullman, Washington

Oxygen Versus Iron Terminations in Hematite Basal Surfaces: Scanning Tunneling Microscope Imaging in Air and Aqueous Solutions

AG Stack
University of California, Davis, Davis, California

Mechanisms of Iron Biomineralization Induced by Dissimilatory Iron Reduction

CM Hansel, S Fendorf
Stanford University, Stanford, California

Mineralogical Analysis of Substrates and End-Products of Microbial Iron Redox Transformations

EE Roden
University of Alabama, Tuscaloosa, Tuscaloosa, Alabama

Solid Phase Characterization/Speciation of Uranium in Hanford 300 Area Sediments

RJ Serne
Pacific Northwest National Laboratory, Richland, Washington

Contaminant-Organic Complexes: Their Structure and Energetics in Surface Decontamination Processes

CL Barajas
Ohio State University, Columbus, Ohio
SJ Traina
University of California, Merced, Merced, California
NP Qafoku, CC Ainsworth
Pacific Northwest National Laboratory, Richland, Washington

Analysis of Clays Reacted with Simulated Hanford Tank Waste
S Choi, JD Chorover
University of Arizona, Tucson, Arizona

Analysis of Iron Mineralogy of Clay Sediments Exposed to Reducing Conditions
DC Cooper
Idaho National Engineering and Environmental Laboratory, Idaho Falls, Idaho

Microbial Reduction of Iron in Sedimentary Clays: Implications for Subsurface Microbial Ecology and Bioremediation
H Dong
Miami University, Oxford, Ohio
RK Kukkadapu
W.R. Wiley Environmental Molecular Sciences Laboratory, Richland, Washington

Formulating the CD-MUSIC Surface Complexation Model from First Principles Calculations for Phosphate Adsorption on Goethite
CJ Tadanier
Virginia Polytechnic Institute, Blacksburg, Virginia

Analyses of Electron Density Distributions in Earth Materials with Implications for Reactivity
GV Gibbs
Virginia Polytechnic Institute, Blacksburg, Virginia

Surface Structure Effects on Direct Reduction of Iron Oxides by *Shewanella oneidensis*
AL Neal
University of Georgia, Aiken, South Carolina

Structure and Reactivity of the Basal and Edge Surfaces of Gibbsite
KM Rosso
Pacific Northwest National Laboratory, Richland, Washington
BR Bickmore
Brigham Young University, Provo, Utah

Environmental Technology Division Laboratory Directed R&D Project for Uranium Sensor Test
W Yantasee
Pacific Northwest National Laboratory, Richland, Washington

The Role of Algae and Bacteria from Berkeley Pit Lake in Metal Sorption Processes
D Bocioaga, GG Mitman
University of Montana, Butte, Montana

Outer-Sphere Electron Transfer Kinetics of Metal Ion Oxidation by Molecular Oxygen

JJ Morgan
California Institute of Technology, Pasadena, California

Critical Point Properties of Electron Density Distributions in High-Pressure Mineral Phases

N Ross
Virginia Polytechnic Institute, Blacksburg, Virginia

Biogenic Iron Mineralization by a Novel Gram-Positive Bacterium: Impact on the Fate of 2,4,6-Trinitrotoluene

WP Inskeep
Montana State University, Bozeman, Montana
T Borch
Stanford University, Stanford, California

Pressure Effect on Electronic Structure of Anthracene Single Crystals: Formation and Modification of Structural Defects

ZA Dreger
Washington State University, Pullman, Washington

Infrared Detection of Organics in Artificial Aging Experiments

CJ Thompson
Pacific Northwest National Laboratory, Richland, Washington

Characterization of Diesel Soot Material by Using Infrared and Raman Spectroscopy

D Kim
Pacific Northwest National Laboratory, Richland, Washington

Gas Chromatography of Solvent Extracted Organo-Phosphorous Compounds from Soils

TA Blake, PL Gassman
W.R. Wiley Environmental Molecular Sciences Laboratory, Richland, Washington

Analysis of Carbon Tetrachloride and Its Degradation Products by Gas Chromatography

JE Amonette
Pacific Northwest National Laboratory, Richland, Washington

The Chemistry and Mineralogy of Variable Charge Soils

NP Qafoku
Pacific Northwest National Laboratory, Richland, Washington

Iron Mineral and Chromium Reduction by *Cellulomonas* Spp.
R Gerlach
Montana State University, Bozeman, Montana
T Borch
Stanford University, Stanford, California

Investigation into the Polarized Raman Spectra of Benzene, Benzene-d6, and Hexafluorobenzene
SD Williams
Appalachian State University, Boone, North Carolina

Measure Fluorescence Spectra from Lithium Fluoride Film
MK Murphy
Pacific Northwest National Laboratory, Richland, Washington

The Aqueous Thermodynamics and Complexation Reactions of Anionic Silica and Uranium Species to High Concentration
HM Cho, AR Felmy, OS Qafoku, Y Xia, Z Wang
Pacific Northwest National Laboratory, Richland, Washington

Highly Selective Monolayer Sorbents for Advanced Analytical Applications
RS Addleman
Pacific Northwest National Laboratory, Richland, Washington
JT Bays, AE Bjerke
U.S. Military Academy, West Point, New York

Isolation of Isotopically Labeled Nucleic Acids
K McAteer
Washington State University, Tri-Cities, Richland, Washington
NG Isern
W.R. Wiley Environmental Molecular Sciences Laboratory, Richland, Washington

Characterization of the Silicon-Carbide/Silicon-Dioxide/Carbon Composite
H Zhang, LS Wang
Washington State University Tri-Cities, Richland, Washington

Multi-Resolution Structure and Reactivity of Kinetically Roughened Oxide Surfaces: Nanometric Scaling Behavior and Molecular-Scale Controls
KM Rosso, EJ Bylaska, S Yanina
Pacific Northwest National Laboratory, Richland, Washington
P Meakin
Idaho National Engineering and Environmental Laboratory, Idaho Falls, Idaho

The Development of Thermodynamic Models for Actinide Species in Mixed Solvent Systems: Application to Binding in Microbial Membranes
SB Clark
Washington State University, Pullman, Washington

Consortium for Agricultural Soils Mitigation of Greenhouse Gases

JE Amonette
Pacific Northwest National Laboratory, Richland, Washington

Center for Research on Carbon Sequestration

JE Amonette
Pacific Northwest National Laboratory, Richland, Washington

Sensor and Tracer Technology for Characterization of Ultra-Low Carbon Dioxide Leakage Fluxes

JE Amonette
Pacific Northwest National Laboratory, Richland, Washington
JL Barr
W.R. Wiley Environmental Molecular Sciences Laboratory, Richland, Washington

Model Porous Solids and Sediments

JE Amonette
Pacific Northwest National Laboratory, Richland, Washington

Biogeochemistry of Uranium Under Reducing and Re-Oxidizing Conditions

JE Amonette
Pacific Northwest National Laboratory, Richland, Washington

Enhancing Carbon Sequestration and Reclamation of Degraded Lands and Sequestered Carbon in Soils

JE Amonette
Pacific Northwest National Laboratory, Richland, Washington

Array-Based Photoacoustic Spectroscopy

JE Amonette, TS Autrey
Pacific Northwest National Laboratory, Richland, Washington
JL Barr
W.R. Wiley Environmental Molecular Sciences Laboratory, Richland, Washington

Carbon Tetrachloride Degradation Reaction Mechanisms

JE Amonette, EJ Bylaska
Pacific Northwest National Laboratory, Richland, Washington
PG Tratnyek, V Sarathy
Oregon Health Sciences University/Oregon Graduate Institute, Beaverton, Oregon

EPA Consulting: MNA of Inorganic Contaminants in Groundwater

JE Amonette
Pacific Northwest National Laboratory, Richland, Washington

A Bioengineering Approach to the Production of Metal and Metal Oxide Nanoparticles

DR Strongin
Temple University, Philadelphia, Pennsylvania

Chemical Speciation of Americium, Curium, and Selected Tetravalent Actinides in High-Level Waste

AR Felmy, Z Wang, OS Qafoku
Pacific Northwest National Laboratory, Richland, Washington

Influence of Reactive Transport on the Reduction of Uranium (VI) in the Presence of Iron (III) and Nitrate

C Liu
Pacific Northwest National Laboratory, Richland, Washington

Interactions Between Iron (III)-Reducing Bacteria and Iron Oxides: Microbial and Geochemical Dissolution Controls

ES Ilton, JM Zachara, KM Rosso
Pacific Northwest National Laboratory, Richland, Washington

Coupling of Iron and Technetium Speciation in Subsurface Sediments: Implications to Long-Term Technetium Immobilization

JM Zachara
Pacific Northwest National Laboratory, Richland, Washington

Mineralogic Residence and Desorption Rates of Sorbed Strontium-90 in Contaminated Subsurface Sediments: Implications to Future Behavior and In-Ground Stability

JM Zachara
Pacific Northwest National Laboratory, Richland, Washington

Impacts of Mineralogy and Competing Microbial Respiration Pathways on the Fate of Uranium in Contaminated Groundwater

JM Zachara
Pacific Northwest National Laboratory, Richland, Washington

Characterization of Uranium (VI) Sorption-Desorption Processes and Model Upscaling

JM Zachara
Pacific Northwest National Laboratory, Richland, Washington
GV Korshin, H Chang
University of Washington, Seattle, Washington

Science and Technology Road Mapping for Needs from All Sources
JM Zachara, Z Wang, M Oostrom
Pacific Northwest National Laboratory, Richland, Washington
TW Wietsma
W.R. Wiley Environmental Molecular Sciences Laboratory, Richland, Washington

Remediation and Closure Science Project/Subsurface Science Tasks
JM Zachara, Z Wang, M Oostrom
Pacific Northwest National Laboratory, Richland, Washington
TW Wietsma
W.R. Wiley Environmental Molecular Sciences Laboratory, Richland, Washington

Hanford Groundwater/Vadose Zone Science Integration
JM Zachara
Pacific Northwest National Laboratory, Richland, Washington

Influence of Mass Transfer on Bioavailablility and Kinetic Rate of Uranium (VI) Biotransformation
C Liu, Z Wang, JM Zachara
Pacific Northwest National Laboratory, Richland, Washington

Reactions and Transport of Toxic Metals in Rock Forming Silicates at 25°C
ES Ilton
Pacific Northwest National Laboratory, Richland, Washington

Actinide Interactions with Environmental Bacteria
MP Neu
Los Alamos National Laboratory, Los Alamos, New Mexico

Characterization of Uranium (VI) Speciation in Samples from Laboratory Batch and Column Experiments
J Wan
Lawrence Berkeley National Laboratory, University of California, Berkeley, Berkeley, California

Liquid Infrared Spectroscopy and Spill Phenomenology
PL Gassman
W.R. Wiley Environmental Molecular Sciences Laboratory, Richland, Washington
RS Disselkamp, JL Hylden
Pacific Northwest National Laboratory, Richland, Washington

Mechanisms and Kinetics of Organic Aging in High-Level Nuclear Waste
TS Autrey, D Camaioni
Pacific Northwest National Laboratory, Richland, Washington

Movement and Dissolution of a Viscous, Multicomponent Light Nonaqueous-Phase Liquid in a Fluctuating Water Table System

C Hofstee
Netherlands Organization for Applied Scientific Research, Utrecht, The Netherlands

Quantification and Chemical Analysis of Iron Oxidation in Microbially Reduced Sediments

RK Kukkadapu
W.R. Wiley Environmental Molecular Sciences Laboratory, Richland, Washington
J Komlos, PR Jaffe
Princeton University, Princeton, New Jersey

Model Development on Using Clay Membranes for Arsenic Removal from Drinking Water

B Deng
University of Missouri, Columbia, Columbia, Missouri

Three-Dimensional Flow and Transport in Highly Heterogeneous Porous Media

BD Wood
Oregon State University, Corvallis, Oregon

Biogeochemical Heterogeneity in the Subsurface

T Resch, PE Long
Pacific Northwest National Laboratory, Richland, Washington

Intermediate Flow Cells

T Resch, JE Szecsody
Pacific Northwest National Laboratory, Richland, Washington

Computational Investigation of Acid Base, Surface Complexation, and Oxidation/Reduction Reaction Mechanisms on Iron Oxide and Iron Silicate Surfaces

JR Rustad
University of California, Davis, Davis, California
AR Felmy
Pacific Northwest National Laboratory, Richland, Washington

The Kinetics of Direct Enzymatic Reduction of Uranium (VI): Effects of Ligand Complexation and Uranium (VI) Speciation

CC Ainsworth, KB Wagnon, Z Wang
Pacific Northwest National Laboratory, Richland, Washington

Enhance Plutonium Mobility During Long-Term Transport Through an Unsaturated Subsurface Environment: Iron and Manganese Oxide Characterization

DI Kaplan
Westinghouse Savannah River, Aiken, South Carolina
BA Powell
Clemson University, Clemson, South Carolina

Uranium Immobilization by Sulfate-Reducing Biofilms

H Beyenal
Montana State University, Bozeman, Montana

Fate of Nitrogen Gas Produced by Denitrification During Uranium and Technetium Bioreduction

JD Istok
Oregon State University, Corvallis, Oregon

Nanoengineered Electrochemical Sensors for Mixed Wastes

Y Lin, Z Wang, W Yantasee
Pacific Northwest National Laboratory, Richland, Washington
X Cui
Eastern Michigan University, Ypsilanti, Michigan

Interfacial Reduction-Oxidation Mechanisms

EC Thornton, JE Amonette
Pacific Northwest National Laboratory, Richland, Washington

How Aluminum Substitution in Goethite Affects Iron Release

J Cervini-Silva, G Sposito
University of California, Berkeley, Berkeley, California

Characterization of Coupled Hydrologic-Biogeochemical Processes Using Geophysical Data

KH Williams
Lawrence Berkeley National Laboratory, University of California, Berkeley, Berkeley, California

Separation of Corn Fiber and Conversion to Fuels and Chemicals: Pilot Operation

DS Muzatko, RJ Orth
Pacific Northwest National Laboratory, Richland, Washington

Investigation of a Barium-Based Nitrogen Oxide Storage-Reduction Catalyst by Raman Spectroscopy

D Kim
Pacific Northwest National Laboratory, Richland, Washington

Influence of Calcium on Aqueous Uranium (VI) Speciation and Uranium (VI) Sorption to the Hanford Sediments

W Ball
Johns Hopkins University, Baltimore, Maryland
C Liu
Pacific Northwest National Laboratory, Richland, Washington

Dissolution and Vaporization of a Mixture of DNAPLs Following a Spill into a Partially Saturated Porous Medium

JH Dane
Auburn University, Auburn, Alabama

Raman Spectroscopy of Silicon Nanowires

R Solanki
Oregon Health Sciences University/Oregon Graduate Institute, Beaverton, Oregon

Uranium (VI) Speciation and Its Influence on Microbial Reduction in Presence of Humic Substances

C Liu
Pacific Northwest National Laboratory, Richland, Washington
B Gu
Oak Ridge National Laboratory, Oak Ridge, Tennessee

Photophysics of Organophosphorous Compounds

AB Padmaperuma, LS Sapochak
Pacific Northwest National Laboratory, Richland, Washington

Influence of Flow on Abiotic and Biotic Reactivity of CL-20 (Hexaanitrohexaazaiso-Wurtzitane)

JE Szecsody, DC Girvin
Pacific Northwest National Laboratory, Richland, Washington

Conductivity of Bacterial Nanowires

YA Gorby
Pacific Northwest National Laboratory, Richland, Washington

Transmission Electron Microscopy Analysis of a Novel Organo-Chromium (III) Degrading Bacterium

GJ Puzon, L Xun
Washington State University, Pullman, Washington

Mössbauer Spectroscopic Investigations of Iron-Doped Tin Oxide Powders

A Punnoose
Boise State University, Boise, Idaho

Synthesis and Characterization of Limited Solubility Uranium (VI)-Bearing Compounds in Concrete

DM Wellman, S Mattigod
Pacific Northwest National Laboratory, Richland, Washington

Staff

Nancy S. Foster-Mills, Senior Research Scientist, Technical Lead
(509) 376-1343, nancy.foster@pnl.gov

Cheryl E. Pomeroy, Administrative Secretary
(509) 376-5362, cheryl.pomeroy@pnl.gov

Paul L. Gassman, Research Scientist
(509) 376-7972, pl.gassman@pnl.gov

Ravi Kukkadapu, Senior Research Scientist
(509) 376-3795, ravi.kukkadapu@pnl.gov

Thomas W. Wietsma, Research Scientist
(509) 376-6588, wietsma@pnl.gov

We would also like to acknowledge the contributions of James E. Amonette, Mark G. Butcher, Eric J. Bylaska, Alice Dohnalkova, Andrew R. Felmy, Eugene S. Ilton, Timothy J. Johnson, Alan G. Joly, Chongxuan Liu, Robert Oor, Martinus Oostrom, Jerry L. Phillips, Odeta Qafoku, Joy D. Rosscup, Kevin M. Rosso, Colleen K. Russell, Zheming Wang, and John M. Zachara.